

An investigation into the effects of anisotropy and  
heterogeneity of fracture permeability on flow and  
thermal transport.

Jesse van der Hoeven

May 19, 2017

## Abstract

To be able to predict the viability of geothermal reservoirs it is important to know how hydrodynamically stimulating a reservoir will alter the system and how fluids will flow through this reservoir. Making an accurate prediction is difficult due to the natural heterogeneity and complexity of the subsurface. In addition, flow through the deep subsurface is often dominated by fractured media rather than by aquifers. This added layer of complexity combined with the inherent difficulties of gathering data in the deep subsurface result in a research field where numerical simulations are crucial. This thesis focusses on the natural heterogeneity of the system and aims to connect the processes on the fracture scale to results on the reservoir scale.

The investigation consists of three sequential parts. Firstly, 2D cases with a single fracture where the effects of fracture wall roughness and shear on the permeability of the fracture are investigated. Secondly, a 3D case with a simple grid to show the effects of fracture with an anisotropic permeability on flow and heat transport. Finally, a 3D simulation to indicate the effects of stress on flow and heat transport through a reservoir.

Shear is found to increase the permeability of a fracture, with the largest increase in the direction perpendicular to the shear. Depending on the initial state of the fracture and the length of shear the permeability perpendicular to the direction of shear is up to one order of magnitude larger compared to the permeability parallel to the direction of shear. This difference can determine whether flow occurs predominantly through the fracture or through the semi-permeable rock matrix.

# Contents

<b>1</b>	<b>Introduction</b>	<b>3</b>
1.1	General introduction and motivation . . . . .	3
1.2	Porous media theory. . . . .	4
1.2.1	Introduction to porous media . . . . .	4
1.2.2	Darcy's law . . . . .	5
1.2.3	Conservation of Mass . . . . .	6
1.2.4	Conservation of Energy . . . . .	7
1.3	Conceptual models. . . . .	8
1.3.1	Modelling fractures in rock matrices . . . . .	8
1.3.2	Fracture mechanical and hydraulic aperture . . . . .	9
1.3.3	Influences of stress on fractures . . . . .	9
1.4	Emperical laws . . . . .	10
1.5	Closing the system . . . . .	10
<b>2</b>	<b>Simulations</b>	<b>12</b>
2.1	Simulation programs,modules and sequence . . . . .	12
2.1.1	Creating a grid with defined fractures . . . . .	13
2.1.2	Preparing the grid for flow calculations . . . . .	13
2.1.3	Solving flow: incompressible two point flux approximation . . . . .	13
2.1.4	Transforming flow to thermal transport . . . . .	14
<b>3</b>	<b>Results and discussion</b>	<b>16</b>
3.1	Effects of shear and initial fracture wall anisotropy on permeability . . . . .	16
3.1.1	2D single fracture modelling details . . . . .	16
3.1.2	2D single fracture results and discussion . . . . .	19
3.2	Effect of fracture presence in 3D with anisotropic permeability . . . . .	28
3.2.1	3D simple network modelling details . . . . .	28
3.2.2	3D simple network convergence test . . . . .	34
3.2.3	3D simple network results and discussion . . . . .	34
3.3	Effect of stress on a fracture network with anisotropic permeability . . . . .	47
3.3.1	3D complex fracture network modelling details . . . . .	47
3.3.2	3D complex fracture network results and discussion . . . . .	52
<b>4</b>	<b>Conclusions</b>	<b>61</b>

# Chapter 1

## Introduction

### 1.1 General introduction and motivation

In the light of the runaway greenhouse effect the request for green and sustainable energy sources is high. One such green energy source is geothermal energy, using the immense amount of heat stored in the earth as a power source. Applications differ between using already surfacing boiling water in, for example, Iceland and New Zealand and utilizing anywhere present the thermal gradient (average 25K/km) of the earth's crust. The groundwater located in deep aquifers or fractured bedrock multiple kilometres below the surface can be won and can already be above boiling temperature, resulting in minimal extra energy needed to convert it to steam to be used in steam powered generators. However, since the recharge rates of these deep aquifers are usually too small to make this commercially viable these reservoirs often need to be anthropogenically stimulated to increase the reservoir permeability [13]. This is usually achieved by hydrodynamically stimulating the reservoir prior to extraction and during extraction maintaining injection rates equal to the extraction rates. This hydrodynamic stimulation involves increasing the pressure in the reservoir to force open already existing fractures, which can cause induced seismicity [14]. Once fractures are opened the permeability of the reservoir increases significantly causing the injection and extraction rates to be viable without immediate significant lowering of the reservoir temperature.

This hydrodynamic stimulation often results in slip of the fracture walls as it lowers the effective normal stress on the fracture. The slip tendency( $T_s$ ) of a fracture is defined as

$$T_s = \tau / \sigma_{neff} \geq \mu_s, \quad (1.1)$$

where  $\tau$  is the shear stress,  $\sigma_{neff}$  is the effective normal stress, defined as the normal stress minus the fluid pressure and  $\mu_s$  is a slip coefficient [14]. When slip occurs the fracture walls are sheared. The effects of anthropogenically inducing shear on the fracture's permeability depend on the initial state of the fracture. The fracture wall surface roughness, determined by the geological history of

the fracture, can create pathways for flow to occur in advantageous conditions but a disadvantageous surface roughness can create blocking fractures where no flow can occur. The influence the fracture surface wall roughness has on the permeability is dependent on the fracture aperture; The more open the fracture is the less influence the walls have on flow through the fracture [20].

However, since this process takes place in the deep subsurface gathering data is expensive and rarely provides a completed image. This combined with the heterogeneity of the subsurface causes this to be an interesting topic of research. Predicting the viability of these reservoirs, in terms of viable extraction rates and decrease in temperature over time, can be done using numerical models. To properly model these reservoirs, techniques for accurate modelling of these stimulated fractures is important since these play a major role in determining the permeability of the reservoir[2]. In addition, smaller not stimulated fractures still play a role in the transport of groundwater and thus heat. Modelling of these smaller fractures can grant better insight into the decrease in temperature over time of these reservoirs.

The focus of this thesis will be the heterogeneity and anisotropy of the fractures. I will start by presenting the theory that will serve as a basis for the simulations. Next, I will delve into the numerical details. Then I will present results from a 2d single fracture simulation I have done to convert mechanical aperture to a Darcy scale permeability. Following this, a simple multiple fracture 3d simulation will be shown with permeabilities based on the 2d simulations. This simple model will show the effects the fractures have on flow and heat transport compared to a general matrix with a significantly lower permeability. Finally, I will show a complex 3d fractured system with an anisotropic permeability distribution based on realistic stress fields. This will visualize the effects of anisotropic fracture permeabilities on the reservoir scale.

## 1.2 Porous media theory.

### 1.2.1 Introduction to porous media

When talking about porous media we are referring to a system of connected pores consisting of pore bodies and pore throats. These pores are void space in an existing system. This system can be made of rock, but also human tissue or even diapers. Porous media on the pore scale are very heterogeneous when it comes to for example pore body and throat size and connectivity of the pore bodies all of which influence flow. However, this heterogeneity disappears if we increase the scale to a representative elementary volume (REV) as visualized in Figure 1.1. The REV is defined as the volume where the parameters defining the porous media do not vary if you slightly change the position where you're looking at the porous media or the volume of your sample. REV values for porous media include porosity, permeability, density and stress, among other things. Just like we define an REV for the matrix, we also define an REV for the fluid to obtain values like the viscosity and the density. When increasing

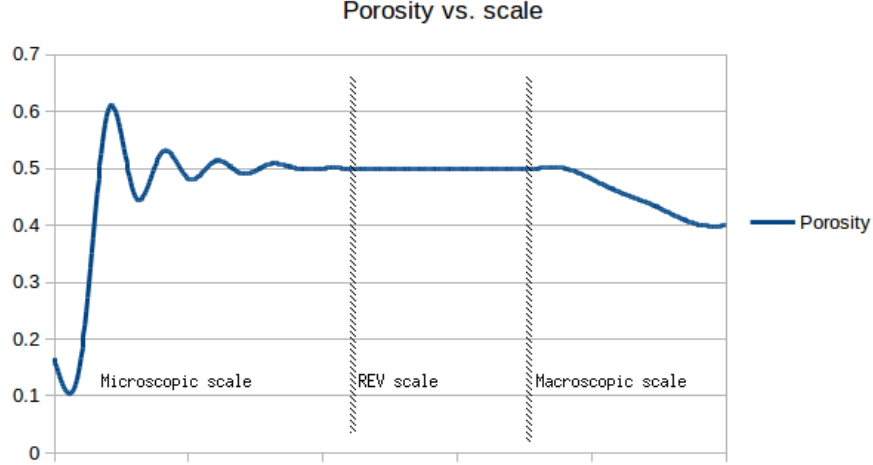


Figure 1.1: The porosity as a function of the scale of a sample. As shown the porosity varies on both the macro- and microscopic scale, but not on the REV scale.

the sample volume far beyond the REV we will start to see differences in these values again. These macroscopic differences can easily be defined in models.

For the purposes of flow simulations only the connected pores are interesting so instead of the porosity we will use the effective porosity, hereafter called the porosity, which is defined as

$$\phi = \frac{V_e}{V_T}, \quad (1.2)$$

where  $\phi$  is the porosity ( $-$ ),  $V_e$  is the empty pore space of the connected pores ( $m^3$ ) and  $V_T$  is the total volume ( $m^3$ ).

### 1.2.2 Darcy's law

To model flow through porous media Darcy's law is used. It required REV values and so cannot be used below that scale. For the purposes of this thesis we will assume that the density of the fluid is constant so we can define Darcy's law [4] as

$$Q = -\mathbf{k} \frac{A \rho g}{\mu} \nabla h, \quad (1.3)$$

where  $Q$  is the volumetric flux ( $m^3/s$ ),  $\nabla h$  is the hydraulic head gradient ( $-$ ),  $\mu$  is the viscosity ( $Pa \cdot s$ ),  $A$  is the cross-section area ( $m^2$ ) and  $k$  is the permeability ( $m^2$ ). For the purposes of this thesis we will be investigating the effects an

anisotropy in the permeability. This will be done by using a vector to define the permeability. That way the fluid will act differently depending on which directional axis, or combination thereof, is followed.

Hydraulic head is defined as

$$h = \frac{P}{\rho g} + z, \quad (1.4)$$

where  $P$  is the pressure (Pa),  $\rho$  is the density of the fluid ( $kg/m^3$ ),  $g$  is the gravitational acceleration constant ( $m/s^2$ ) and  $z$  is the elevation level (m). Since I will be working with pressure driven flow and will neglect the effects of gravity we can rewrite Darcy's law to

$$Q = -\mathbf{k} \frac{A}{\mu} \nabla P \quad (1.5)$$

or

$$\mathbf{q} = -\frac{\mathbf{k}}{\mu} \nabla P, \quad (1.6)$$

where  $\nabla P$  represents an effective pressure difference which includes the effects of differences in elevation and  $\mathbf{q}$  represents the darcy flux ( $m/day$ ). We can include the effects of gravity in this equation because we're assuming the density of the fluid to be constant. The darcy flux relates to the average velocity ( $\mathbf{v}$ ) of the fluid flow according to the equation

$$\mathbf{v} = \frac{\mathbf{q}}{\phi}. \quad (1.7)$$

Important to note is that Darcy's law is only valid for low velocity values where flow is laminar, up to the  $m/day$  scale but since this is the case for most flow through porous media we will assume this to be the case in this thesis.

To clearly map the impacts of flow velocity and when the fluid reaches which parts of our model we can use the time-of-flight. Time-of-flight is defined as the time it takes for a particle coming into the model to reach a certain point inside of the model.

When talking about permeability the unit of Darcy ( $D$ ), milliDarcy ( $mD$ ) and even microDarcy ( $\mu D$ ) is often used. One Darcy is equal to a permeability of about  $10^{-12} m^2$ . For typical example permeability values see Table 1.1.

### 1.2.3 Conservation of Mass

Mass conservation is a principle upon which flow solvers are based. It states that the mass of a closed system will remain constant and when mass through a source enters the system an equal amount of mass has to either be stored in the system or leave the system through a sink. In this thesis we will assume

Permeability ( $D$ )	Permeability( $m^2$ )	Example	Example
$k = 10^4 D$	$k = 10^{-8} m^2$	Gravel	Highly fractured bedrock
$k = 10^1 D$	$k = 10^{-11} m^2$	Sorted sand	Oil reservoir rock
$k = 1 D$	$k = 10^{-12} m^2$	Fine sand	Peat
$k = 10^{-2} D$	$k = 10^{-14} m^2$	Layered clay	Sandstone
$k = 10^{-6} D$	$k = 10^{-18} m^2$	Unweathered clay	Unfractured granite

Table 1.1: Examples of typical permeabilities found in nature. When modelling flow through rock it is visible that the permeability can vary greatly depending on the situation of the bedrock as the difference between a highly fractured rock and an unfractured rock can be 10 orders of magnitude.

both the fluid and the rock matrix to be incompressible. This means there can be no additional mass stored in the system which results in the equation

$$\frac{d}{dt} \int_V m dV = - \int_A \mathbf{q} \cdot \hat{\mathbf{n}} dA + \int_V s dV, \quad (1.8)$$

where  $\hat{\mathbf{n}}$  represents the outward normal vector where the fluid exits the system and  $s$  represents the sources. When we assume the fluid and matrix are both incompressible, we can simplify this equation to

$$\frac{dm}{dt} = -\nabla \cdot \mathbf{q} + s. \quad (1.9)$$

Since we will be working with a single fluid phase the mass can be written as  $m = \phi \rho$ . Both porosity and density are assumed to be constant, removing the derivative term in equation (1.9). The flow in the system relates to  $\mathbf{k} \cdot \nabla P$  in the system according to equation (1.5), when we assume the viscosity to be constant. The conservation of mass can now be written as

$$s = \nabla \cdot \left( \frac{\mathbf{k}}{\mu} \nabla P \right), \quad (1.10)$$

which gives us a pressure and flow field used when simulating flow.

### 1.2.4 Conservation of Energy

In addition to mass conservation we will also apply energy conservation. This law will allow us to solve the simulations for temperature transport. Conservation of energy is defined as

$$\frac{\partial E}{\partial t} + \nabla \cdot \mathbf{J} = f, \quad (1.11)$$



where  $E$  is the energy of the system,  $t$  is time,  $J$  is the energy flux and  $f$  represents the sources and sinks of the system. The energy term in this equation is used as a combination between potential, kinetic and internal energy. For the purposes of this thesis we will assume the kinetic energy to be negligible since we're investigation flow in the subsurface where flow velocities are minimal and the effects of gravity are included in our Darcy equation. The resulting internal energy can be used to describe the temperature of the system since we're assuming no phase changes and an incompressible fluid. This is correlated using the equation

$$du_{internal} = c_p dT, \quad (1.12)$$

where  $du_{internal}$  is the change in internal energy,  $c_p$  is the heat capacity and  $dT$  is the change in temperature.

The energy flux consists of the advective flux and the diffusive flux. These fluxes are described as

$$\mathbf{J}_{adv} = \mathbf{q}T, \quad (1.13)$$

$$\mathbf{J}_{dis} = -D\nabla T, \quad (1.14)$$

where  $D$  is the thermal diffusion coefficient. If we insert this in equation (1.11) and we assume that energy loss from the fluid into the rock is minimal we get the equation

$$\frac{\partial T}{\partial t} = f - \nabla \cdot (\mathbf{q}T) + \nabla \cdot (D\nabla T). \quad (1.15)$$

## 1.3 Conceptual models.

### 1.3.1 Modelling fractures in rock matrices

When modelling rock the REV approach can often not be enough due to the presence of fractures in the rock. These fractures can be any size and can significantly influence the permeability. In the case of smaller fractures their effects can be small enough and their distribution large enough for the REV approach to still work, but for the larger fractures the local permeability can increase drastically. This causes the REV approach to be lacking, especially since fractures have a diminutive height compared to their width and length. To be able to use the REV approach while also properly modelling fractures they are often modelled as a lesser dimensional object, a one dimensional line in a two dimensional plane and a two dimensional plane in a three dimensional grid.

These fractures, formed by stress and shearing of the bedrock, can be open or closed and therefore can either drastically increase local permeability or drastically decrease local permeability.

### 1.3.2 Fracture mechanical and hydraulic aperture

Once these fractures are sheared they will be opened on certain parts and closed on other parts. The distance between the two fracture walls is defined as the mechanical aperture. The aperture of a fracture depends on the normal load stress of the fracture, the more stress the lower the aperture. This results in fractures in the upper subsurface having relatively large apertures and deep fractures having relatively small apertures. In addition to this the orientation of the fracture can affect the aperture since the orientation can affect the normal load stress. A vertical fracture will likely have a higher aperture than a horizontal fracture [1].

The hydraulic aperture is used as an effective distance between the fracture walls that is used for flow [17]. This is not equal to the mechanical aperture since flow depends on the bottlenecks of the fracture instead of simply the average distance between the two fracture walls. Since the hydraulic aperture is a value originated from the physical attributes of the fracture that directly affects flow it can be translated to permeability using the equation

$$k = \frac{1}{12} e_h^2, \quad (1.16)$$

where  $e_h$  is the hydraulic aperture (m). In literature fractures are often simplified as two smooth surfaces separated by the aperture of the fracture. This is a simplification that allows a lot of mathematical work to be done on flow through fractures but does not account for fracture wall roughness and anisotropy of the fracture. The difference between mechanical aperture and hydraulic aperture is a way to correct this.

### 1.3.3 Influences of stress on fractures

The average fracture aperture is determined by the effective normal stress, which is the normal stress of the rock minus the fluid pressure. The lower the effective normal stress, the less contact is needed between the fracture walls to provide the normal forces that counter the forces from the effective normal stress. This results in a higher average fracture aperture and thus a higher permeability. These areas of contact between the fracture walls also provide shear resistance by increasing the slip coefficient. The more contact, the more force required to shear the fracture. When shear happens one fracture wall moves with respect to the other fracture wall. The length of this movement is known as shear displacement.

An increase in shear displacement results in an increase in both the mean aperture and the standard deviation of the aperture of the fracture [6]. The resulting increase in permeability is largest perpendicular to the direction of shear [12].

An increase in fluid pressure results in a decrease in effective normal stress which results in a decrease in shear resistance which can produce shear in the fracture. Due to the roughness of the fracture walls this shear can produce opening of the fracture which can result in an increase in permeability. The greater

the shear displacement the higher the increase in permeability [19]. However, the shear displacement is determined by both the shear stress vs. shear resistance and the length of the fracture[21]. Therefore, a smaller fracture results in a smaller shear displacement which results in a lower increase of the permeability. This is why we only explicitly model the larger fractures in the system, the change in the smaller fractures is insignificant compared to the change in the larger fractures.

In addition to determining the aperture of the fracture the stress field can also determine the permeability tensor by influencing the prevalent fracture anisotropy and orientation. This can determine flow paths and thus the volume of rock where heat is taken from and the duration of transport [5].

## 1.4 Emperical laws

It is known that an increase in mechanical aperture will result in an increase in permeability. However, at the time of writing there is no equation clearly describing this bond. Instead, we must use emperically found equations. First of all, we need to translate mechanical aperture to hydraulic aperture. In [15] this was investigated and the following formula was found:

$$e_h = 0.2 \cdot e_m, \quad (1.17)$$

where  $e_m$  is the mechanical aperture (m).

Fracture aperture and contact area is determined by the effective normal stress on the fracture. This in turn is mostly determined by the depth of the fracture. For the purposes of this thesis we will look at two different situations. A fracture with an average effective normal stress of 0.45 MPa representing a depth in the scale of meters, from here on to be refered to as a shallow fracture, and a fracture with an average effective normal stress of 35 MPa representing a depth in the scale of kilometers, from here on to be refered to as a deep fracture.

## 1.5 Closing the system

The simulations are preformed by solving Equations (1.10) and (1.15) for a domain  $\Omega$  with boundary  $\partial\Omega$ . During this thesis we will assume Dirichlet boundary conditions on the inlet and the outlet boundary conditions of the model and no flow on the other boundaries. When wells are introduced all boundaries are defined as no flow and the temperature equation is solved by introducing injection temperature  $T_1$  in the injection well. To summarize, the equations that need to be solved are

$$\nabla \cdot \left( \frac{\mathbf{k}}{\mu} \nabla P \right) - s = 0 \text{ in } \Omega,$$

$$\mathbf{q} = -\frac{\mathbf{k}}{\mu} \nabla P \text{ in } \Omega,$$

$$\frac{\partial T}{\partial t} = f - \nabla \cdot (\mathbf{q}T) + \nabla \cdot (D\nabla T) \text{ in } \Omega,$$

with boundary conditions

$$P = P_1 \text{ on } \partial\Omega_{in},$$

$$P = P_0 \text{ on } \partial\Omega_{out},$$

$$\mathbf{q} \cdot \hat{\mathbf{n}} = 0 \text{ on } \partial\Omega_{rest},$$

$$T = T_1 \text{ at } \partial\Omega_{in},$$

$$T = T \text{ at } \partial\Omega_{rest}$$

and initial condition

$$T = T_0 \text{ in } \Omega \text{ at } t = 0.$$

where  $\mu$ ,  $D$  and  $\mathbf{k}$  are material properties and  $P$ ,  $\mathbf{q}$  and  $T$  are the variables to be solved for. Furthermore,  $P_1$  and  $P_0$  are the pressure at the inlet and outlet boundary respectively and  $T_0$  is the initial temperature of the system. Finally,  $t$  is time,  $f$  and  $s$  are source terms and  $\hat{\mathbf{n}}$  is the outgoing normal vector. Since there are five variables and five equations we can solve this system.

## Chapter 2

# Simulations

The simulations in this thesis will be done in a sequential manner. First we will solve for pressure driven flow, followed by thermal transport. This can be done since we are working with incompressible fluid and rock. Using an imposed pressure difference through equation (1.10) we will obtain the pressure per cell, the flux per cell face and the time-of-flight per cell. The flux per cell face from this equation can be used to solve equation (1.15) to obtain the temperature per cell over time.

### 2.1 Simulation programs, modules and sequence

To do the simulations required for this thesis the Matlab Reservoir Simulator Toolbox (MRST) will be used [16]. Within MRST certain modules exist to better simulate the specific flow problems we will be looking at. For the flow simulations the `incompTPFA` (incompressible two point flux approximation) module is used and to discretize the fractures we will use the `DFM` (discrete fracture matrix) module.

While the simulations are done in MATLAB, it is not the only program used for this thesis. When creating unstructured grids the program `Gmsh` is used [7]. `Gmsh` is a three-dimensional finite element grid generator. Through MATLAB files are generated detailing the boundaries, the cell sizes and the locations of the fracture planes in the grid and `gmsh` combines these parameters to create a single grid with 3d and 2d geometries.

After the 3d flow simulations are done the 3d visualization of the results is done in `Paraview` [10]. `Paraview` is a visualization tool designed to analyze large datasets. Through MATLAB a file is generated detailing the grid and any to be visualized parameters, such as pressure, time-of-flight and velocity vectors.

### 2.1.1 Creating a grid with defined fractures

To create an unstructured grid with fractures Gmsh needs certain parameters to be prepared with MATLAB. First of all the boundaries of the model are required. For every dimension a minimum value and a maximum value is created. Second, the fractures are defined. When working in 3d the fractures are 2d planes and when working in 2d the fractures are 1d lines. This is done by supplying the corner points between which the fracture plane is located. During this thesis every fracture will consist of four corner points to create trapizoidal fractures. Finally, a parameter describing the size of the cells for the matrix and a parameter describing the size of the fracture cells are required. These parameters can be different to provide more detail in the fractures for better investigation. When this is the case Gmsh will shrink the matrix cells in contact with and close to the fracture to fit to the size of the fracture cells themselves. The grid created in this way will consist of multiple 2d geometries existing within a single 3d geometry.

The geometries are combined into one using the MATLAB DFM module. The planes corresponding to the fracture elements are assigned an aperture to artificially give them a volume so they can be used for the flow calculations.

### 2.1.2 Preparing the grid for flow calculations

To use this complex grid for flow calculations the multiple geometries need to be combined into one and every cell needs to be able to act like a cell of the upper dimensional geometry for the purposes of flow simulations. The DFM module will combine the grid into one geometry while preparing the lower dimensional cells for flow simulations by assigning an aperture. This aperture is an arbitrary length assigned normal to the fracture cell used to calculate an arbitrary cell volume, or area when simulating in 2d, in the cell. By having a volume the cell can be used as an upper dimensional cell for the purposes of flow simulations.

Once this is done a porosity and permeability can be assigned for every cell and converted into a transmissivity per cell face and a volume of empty space per cell.

### 2.1.3 Solving flow: incompressible two point flux approximation

The incompTPFA module is used to solve for flow. It uses the transmissivity per cell face calculated from the permeability to calculate the flux between two cells, with inputs coming from boundary conditions or wells in the shape of either pressure driven or flux driven flow. As the name suggests the TPFA method uses two points of average cell pressure to approximate the flux through the face between those two cells. From the incompTPFA we gain the pressure per cell, the flux per interface and when using wells the flux and pressure in the wells. From this result the time of flight can be calculated through the computeTimeOfFlight method found in mrst.

However, there is a possible issue when combining the incompTPFA module, an unstructured grid and an anisotropic permeability. In an unstructured grid the normal vector between two cells can always vary. The calculation of a normal vector for two adjacent cells is as

$$\hat{\Delta n} = \begin{pmatrix} \hat{\Delta x} \\ \hat{\Delta y} \\ \hat{\Delta z} \end{pmatrix} = \frac{\begin{pmatrix} x_n \\ y_n \\ z_n \end{pmatrix} - \begin{pmatrix} x_{n+1} \\ y_{n+1} \\ z_{n+1} \end{pmatrix}}{\left\| \begin{pmatrix} x_n \\ y_n \\ z_n \end{pmatrix} - \begin{pmatrix} x_{n+1} \\ y_{n+1} \\ z_{n+1} \end{pmatrix} \right\|}, \quad (2.1)$$

where  $x_n, y_n, z_n$  represent the coordinates of a cell,  $x_{n+1}, y_{n+1}, z_{n+1}$  represent the coordinates of an adjacent cell and  $\hat{\Delta n}$  represents the unit vector showing the direction from one cell center to another. This grants a lot of advantages when compared to a structured grid, in the case of this thesis the ability to investigate fracture networks where the fractures are in any orientation with respect to each other and not just perpendicular. However, when using an anisotropic permeability the transmissivity for each cell face is calculated from a combination of the permeability in each direction and the angle the cell face has with this directional axis. The larger the angle with the directional axis the less influence the permeability in that directional axis has, up to an angle of  $\frac{1}{2}\pi$  where the influence is 0. This means that if there is a large difference between the directional permeabilities a small deviation from one directional axis can cause a large increase in the transmissivity of the cell face.

$$T_{\Delta n} = \hat{\Delta n} \cdot \begin{pmatrix} k_x \\ k_y \\ k_z \end{pmatrix}, \quad (2.2)$$

where  $k_x, k_y, k_z$  represent the permeabilities in the different axial directions and  $T_{\Delta n}$  represents the transmissivity of the cell face separating the two cells  $n$  and  $n+1$ . For example, when we have  $\Delta x = 0.1\Delta y$  but  $k_x = 100k_y$  and  $\Delta z = 0$  our transmissivity becomes  $T_{\Delta n} = \Delta x k_x + \Delta y k_y = 10\Delta y k_y + \Delta y k_y = 11\Delta y k_y$ . This large difference with a small deviation from the directional axis can cause larger errors in the model so it is recommended when using an unstructured grid and the incompTPFA module to use permeabilities with differences within one order of magnitude.

#### 2.1.4 Transforming flow to thermal transport

Finally, from the results of the incompTPFA method the temperature per cell over time can be calculated. Due to the large difference in permeability in the fractures and in the matrix an explicit discretization would require an enormous amount of time steps and computational power. Therefore, an implicit temperature solver is required as this is unconditionally stable in time. We can write equation (1.15) in our grid as

$$\frac{\partial T_i}{\partial t} + \sum_{f=1}^{m_i} \mathbf{q} T_{upw} - D_{ij}(T_j - T_i) = f_i, \quad (2.3)$$

where  $i$  and  $j$  are cell indices and  $T_{upw}$  is the temperature in the upwind cell,  $i$  or  $j$ , depending on the direction of the flux  $\mathbf{q}$ . After implicit discretization the temperature per cell for every time step can be solved using the equation

$$\frac{T_i^{t+1} - T_i^t}{\Delta t} + \sum_{f=1}^{m_i} \mathbf{q} T_{upw}^{t+1} - D_{ij}(T_j^{t+1} - T_i^{t+1}) = f_i^{t+1}, \quad (2.4)$$

where the superscript  $t$  represents the time step.



## Chapter 3

# Results and discussion

The simulations shown in this chapter are done following Figure 3.1. Starting with inputs that affect a single fracture we will apply upscaling to end up with a conclusion that affects a fracture network.

### 3.1 Effects of shear and initial fracture wall anisotropy on permeability

We will start by investigating the effects of shear on permeability in a single fracture. The permeability is calculated from the hydraulic aperture, which is a consequence of the roughness of the surface walls of the fracture. This aperture is manipulated by altering initial conditions and the direction and magnitude of shearing. As an output we take the permeability of the system as a whole, calculated from flow results.

#### 3.1.1 2D single fracture modelling details

The single fracture model is a 90x90 cartesian grid representing a 30x30mm part of a fracture. A 120x120 Gaussian surface [8] is generated with median set to 250  $\mu m$  and the standard deviation set to 150  $\mu m$  to produce results found in literature [9]. The gaussian surface is 120x120 to account for the induced shear as this 30 cell margin will be used to make sure the cells at the borders of the model use values that are connected through the correlation length. The correlation length is varied in the y-direction to create an anisotropic system with an anisotropy ratio ( $\eta$ ) defined as

$$\eta = \frac{Corr_x}{Corr_y}, \quad (3.1)$$

where  $Corr_x$  is the correlation length in the x-direction and  $Corr_y$  is the correlation length in the y-direction. The direction of anisotropy is in the x-direction when  $\eta > 1$  and in the y-direction when  $\eta < 1$ . Four different values of  $\eta$  are

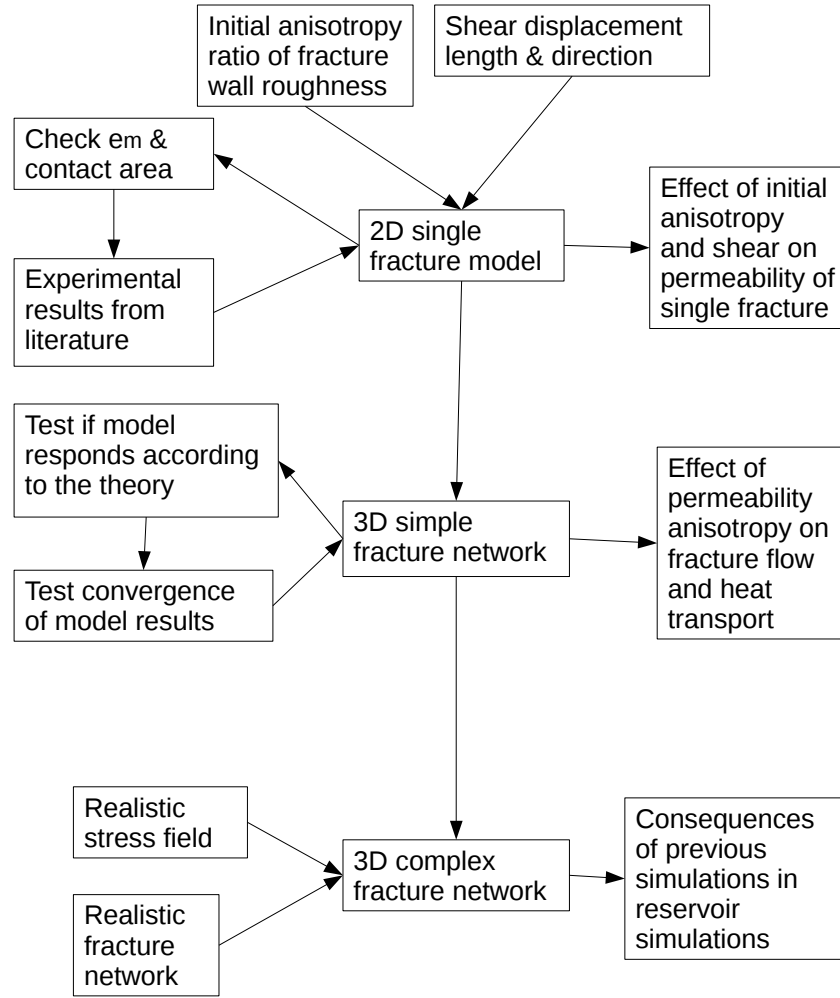


Figure 3.1: Visualization of the simulation inputs, outputs and iterations. The inputs are at the top and the bottom left hand side, the outputs on the right hand side and the iterations on the top and middle of the left hand side of the figure.

tested: 10, 5, 2 and 1. 1 represents an isotropic fracture and 10 represents a highly anisotropic fracture. For the purposes of this thesis the  $Corr_x$  is always set to 30 cells or 10mm and the  $Corr_y$  is varied. An example of an anisotropic surface generated this way is shown in Figure 3.2. This surface is copied and shifted in the  $x$ -direction, 3 cells per millimeter of shear length, and subtracted from the initial surface. For the purposes of this thesis this shear direction will be labeled as parallel (||) shear from now on. For every different anisotropic situation five different shear displacements, or shear lengths ( $S_L$ ) are investigated: 1mm, 2mm, 3mm, 5mm and 10mm. The largest negative point is taken and multiplied by a factor representing a shallow or deep fracture. When applying parallel shear this process is described by the equations (3.2) and (3.3).

$$dH = F \cdot \min(H_{(x,y)} - H_{(x-S_L,y)}), \quad (3.2)$$

where  $F$  is -0.09 for a deep fracture and -0.65 for a shallow fracture,  $H$  is the height generated by the Gaussian function and  $dH$  represents the increase in height of the entire sheared surface. The factor  $F$  is chosen in such a way that the resulting  $e_m$  is representative of values found in experimental studies for fractures with fixed normal load [9, 11]. This generates the mechanical aperture of the entire model through the equation

$$e_m = H_{(x,y)} - H_{(x-S_L,y)} + dH. \quad (3.3)$$

Any negative mechanical apertures are set to 0, representing a closed part of the fracture where flow cannot take place.

Once the mechanical aperture has been defined it can be translated to the permeability per cell through equations (1.17) and (1.16). The top, bottom, upper and lower boundaries are defined as no-flow boundaries, the left hand side of the model is set to a pressure of 1 bar and the right hand side of the model is set to 0 bar so we get pressure driven flow in the  $x$ -direction.

Once the model has been solved for flow the Darcy permeability of the fracture can be found using the cubic law,

$$Q = \frac{\rho \cdot g}{12\mu} \cdot e_h^3 \cdot W \cdot \nabla h, \quad (3.4)$$

where  $W$  is the width of the fracture(m). This can be rewritten using equations (1.16) and (1.4) to find the Darcy permeability based on the volumetric flux.

$$k_d = \frac{Q \cdot \mu}{A \cdot \nabla P}, \quad (3.5)$$

where  $A$  is the area perpendicular to flow and equal to  $e_h \cdot W$ . Important to note is that the cubic law is found using the Navier-stokes equation on flow between two parallel plates without accounting for roughness [3].

The  $dH$ , the percentage of cells where  $e_m = 0$  and the  $k_d$  are taken as a result. Since flow is in the  $x$ -direction  $k_d$  can also be written as  $k_x$ . The  $dH$  and contact area are used to check if the results are representative and the  $k_x$  is stored to use in the 3D simulations.

This process is repeated with shear in the  $y$ -direction, which for the purposes of this thesis will be labeled perpendicular ( $\perp$ ) shear from now on. The surface is then rotated by  $\frac{1}{2}\pi$  radians and both previous simulations are repeated to investigate the permeability in the  $y$ -direction ( $k_y$ ). These four situations represent the following:

1.  $k_x$  with parallel shear.
2.  $k_x$  with perpendicular shear.
3.  $k_y$  with perpendicular shear.
4.  $k_y$  with parallel shear.

This experiment is repeated 100 times for every scenario to provide statistical significance for a total of 8000 simulations.

### 3.1.2 2D single fracture results and discussion

The generated fracture surface is shown in Figures 3.2 and 3.4 for  $\eta = 10$  and 1 respectively. The mechanical aperture distribution from these surfaces after 1 mm of shear is shown in Figures 3.3 and 3.5.

The following results are from the shallow fracture with  $\eta = 10$  and  $S_L = 1$  mm and 10 mm. These are shown to illustrate certain differences in the results clearly. At the end of this paragraph figures from the data from all the other simulations are included.

The single fracture simulations for shallow fractures provided dH as shown in Figures 3.6 and 3.7 and contact area as shown in Figures 3.8 and 3.9.

When comparing Figures 3.6 and 3.7 it becomes clear that the average mechanical aperture of the fracture is determined by the shear length and the correlation length. For the case with perpendicular shear there is little difference between the scenario with 1mm of shear, equal to the correlation length in this direction, and 10mm of shear, equal to ten times the correlation length in this direction. For the case with shear parallel to flow this is not the case as the mechanical aperture is seen to increase from the scenario with 1mm of shear, equal to 0.1 times the correlation length, and 10mm of shear, equal to the correlation length. Since the mechanical aperture directly impacts the permeability we can state that increasing the shear length of a fracture will increase the permeability of the fracture until the correlation length is reached.

The observed changes in the contact area are minimal. It appears to rise for the scenario with parallel shear when increasing the shear length though this change when compared to the spread of the data set is minimal. This lack of difference is expected since the contact area depends on the normal stress which does not change when increasing shear length.

After solving for flow the Darcy permeability of the fractures is shown in Figures 3.10 and 3.11.

Two effects are clear when studying these graphs. First, the permeability in the  $x$ -direction is always larger than the permeability in the  $y$ -direction. This is

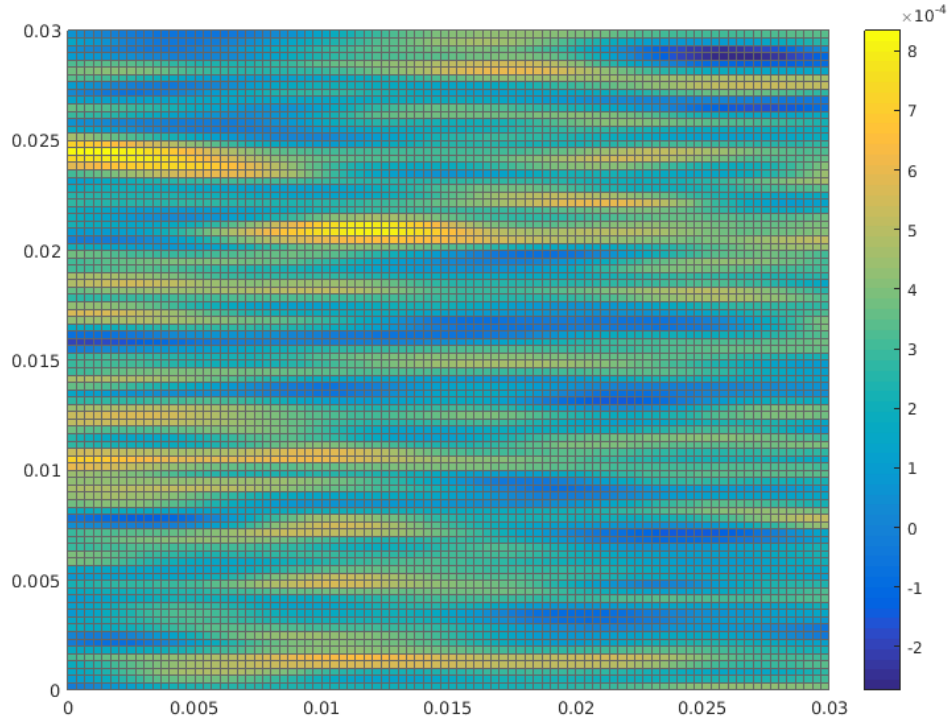


Figure 3.2: The Gaussian distribution of the fracture surface with  $\eta = 10$ . The axes represent the distance in  $m$ . Shown values are apertures in  $\mu m$ . Negative values are present as these will be significant when subtracting from the sheared surface.

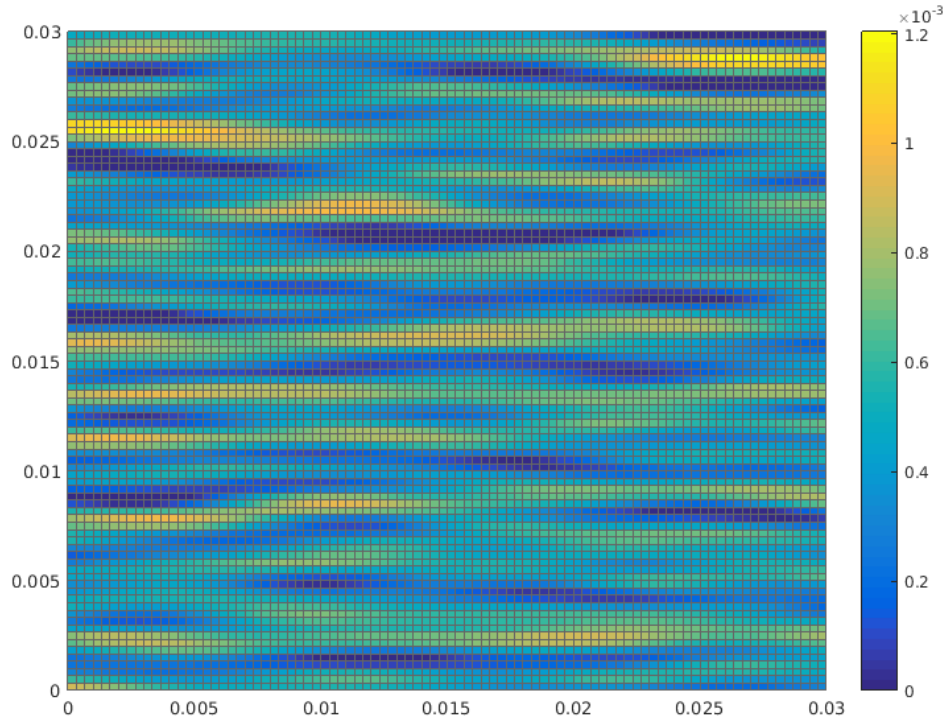


Figure 3.3: The mechanical aperture in  $\mu m$  per cell of the fracture. The axes represent the distance in  $m$ . Clear pathways for flow in the x-direction are visible as a result of the  $\frac{C_{corr_y}}{S_{Ly}} = 1$ . Any negative values after subtraction are set to 0.

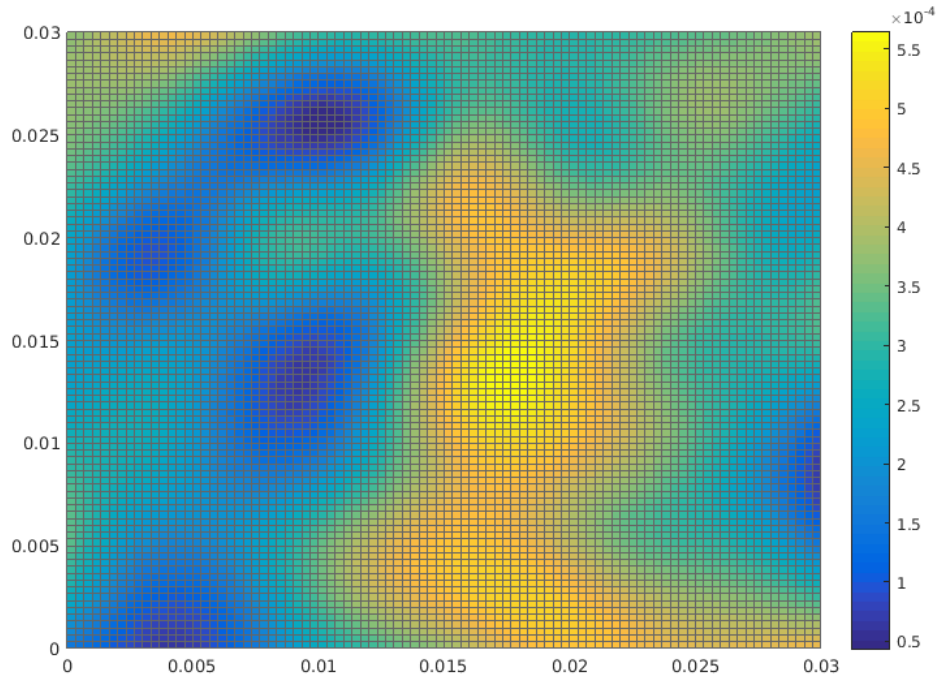


Figure 3.4: The Gaussian distribution of the fracture surface with  $\eta = 1$ . The axes represent the distance in  $m$ . Shown values are apertures in  $\mu m$ . Negative values are present as these will be significant when subtracting from the sheared surface.

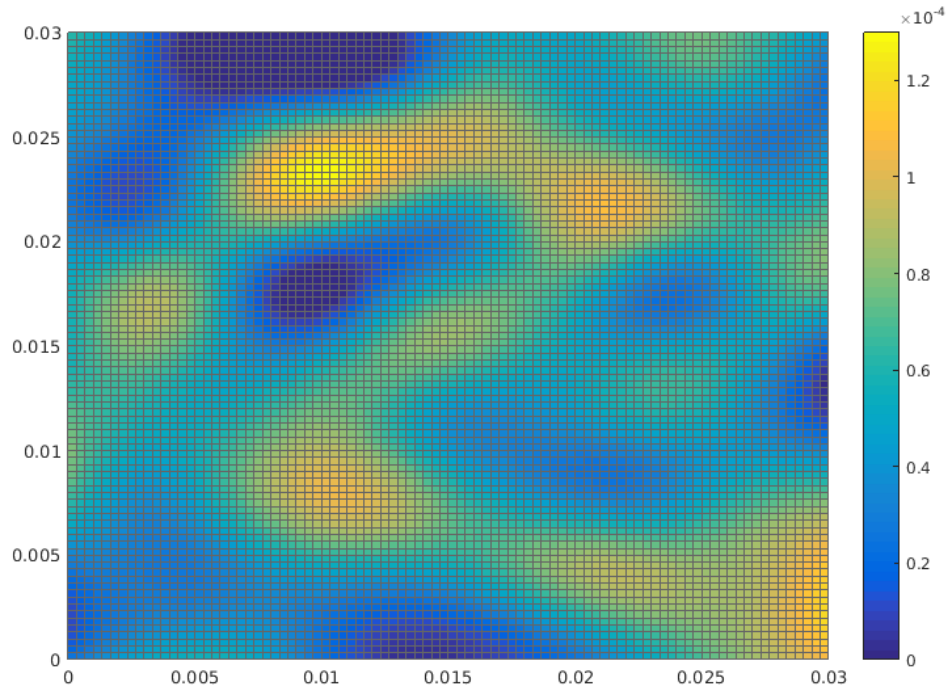


Figure 3.5: The mechanical aperture in  $\mu m$  per cell of the fracture. The axes represent the distance in  $m$ . The values are significantly lower than the values of 3.3. This is because the  $\frac{C_{corr_y}}{S_{Ly}} = 0.1$ . Any negative values after subtraction are set to 0.



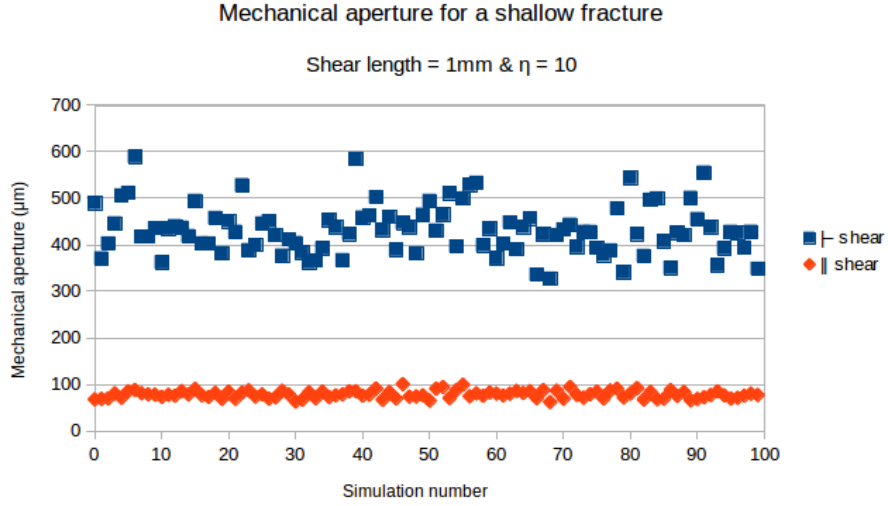


Figure 3.6: Average mechanical aperture per simulation for the scenario's with shear perpendicular to flow ( $\perp$ ) and shear parallel to flow ( $\parallel$ ). The  $\eta$  is set to 10 so when shearing perpendicular to flow the correlation length is reached after 1mm of shear but when shearing parallel to flow the shear length needs to be 10mm before the correlation length is reached.

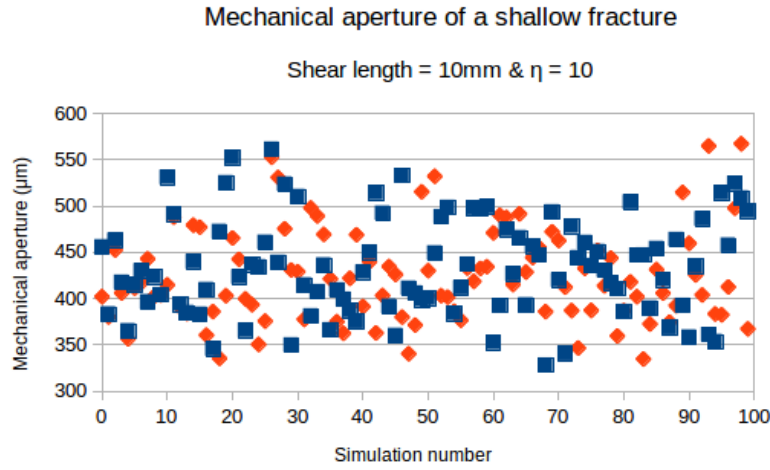


Figure 3.7: Average mechanical aperture per simulation for the scenario's with shear perpendicular to flow ( $\perp$ ) and shear parallel to flow ( $\parallel$ ). The  $\eta$  is set to 10 so when shearing perpendicular to flow the correlation length is reached after 1mm of shear but when shearing parallel to flow the shear length needs to be 10mm before the correlation length is reached.

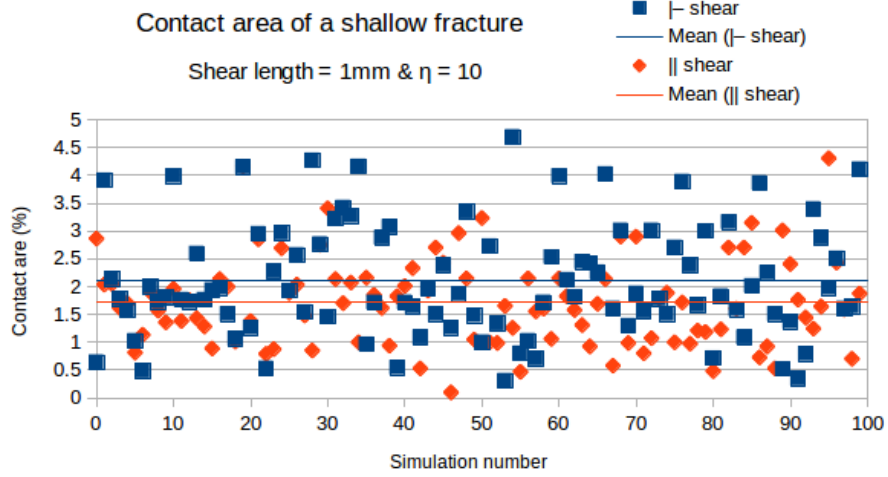


Figure 3.8: The percentage of cells where  $e_{mech} = 0$  per simulation with shear perpendicular to flow ( $\perp$ ) and shear parallel to flow ( $\parallel$ ). A mean line is plotted for clarity for both data sets.

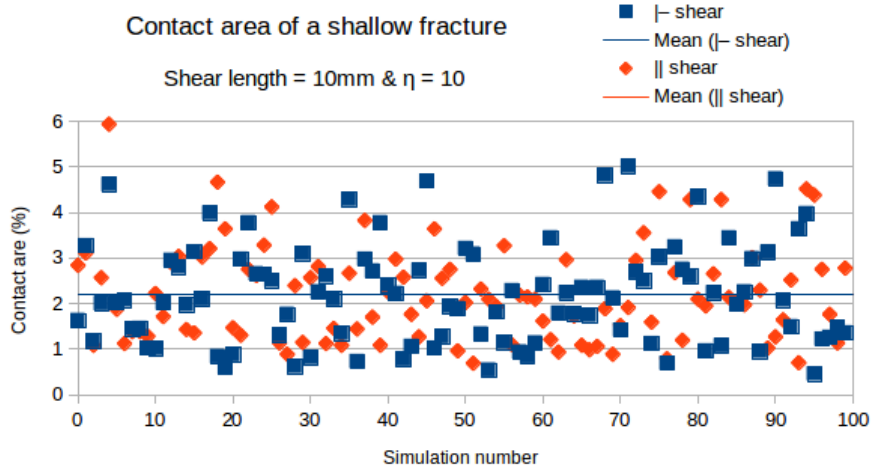


Figure 3.9: The percentage of cells where  $e_{mech} = 0$  per simulation with shear perpendicular to flow ( $\perp$ ) and shear parallel to flow ( $\parallel$ ). A mean line is plotted for clarity for both data sets, though the mean values are so close the red line is completely covered by the blue line.

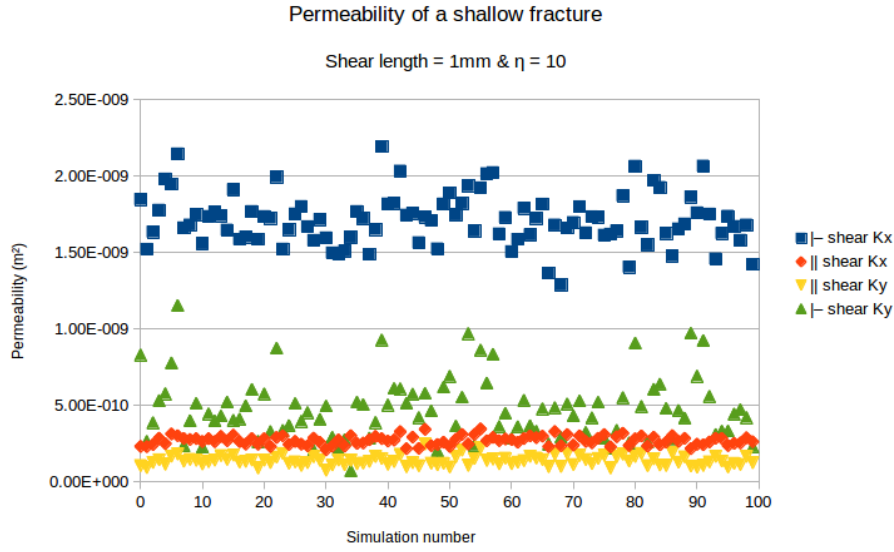


Figure 3.10: Darcy permeability ( $m^2$ ) for a shallow fracture. The  $\perp$  indicates shear is perpendicular to the direction of preferential anisotropy and the  $\parallel$  indicates shear is parallel to the direction of preferential anisotropy. The scenario where shear is perpendicular to flow reaches the correlation length at 1mm of shear, resulting in significantly large permeabilities than the scenario where shear is parallel to flow where 1mm of shear is equal to 0.1 times the correlation length.

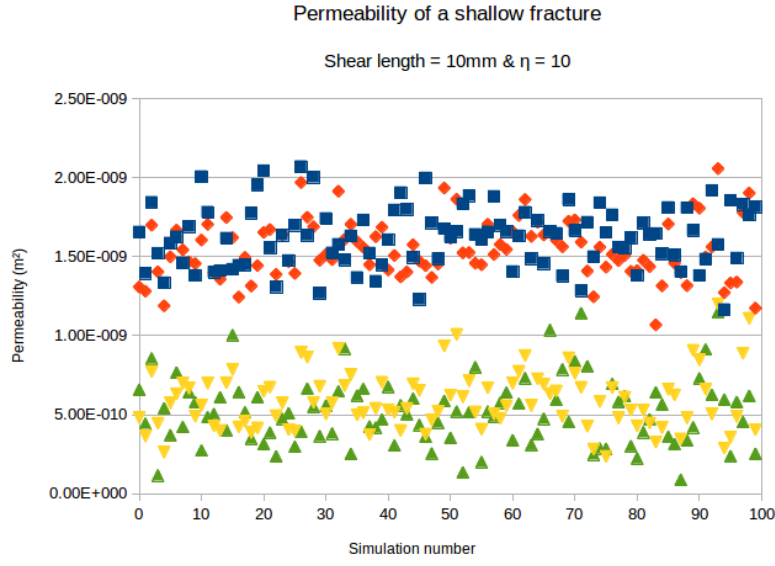


Figure 3.11: Darcy permeability ( $m^2$ ) for a shallow fracture. The  $\perp$  indicates shear is perpendicular to the direction of preferential anisotropy and the  $\parallel$  indicates shear is parallel to the direction of preferential anisotropy. Since the shear length is equal to or large than the correlation length in both scenarios the data sets are quite equal for permeabilities in the same direction.

due to the initial anisotropy of the fracture as this helps the formation of channels for flow in the  $x$ -direction. Secondly, the permeabilities of the simulations with shear parallel to the direction of preferential anisotropy increase drastically with increasing shear length. This is due to the correlation length being reached at shear length = 10mm. In the case where shear is perpendicular to the direction of preferential anisotropy instead of this increase a decrease in permeability with increasing shear length is seen, most notable when comparing the  $|-$  shear  $k_x$  data sets.

These effects are also seen the other scenarios as shown in Figures 3.12, 3.13, 3.14 and 3.15.

When looking at these results we see that the effects of an anisotropic permeability are more outspoken in the deep fractures. These variations are most likely more significant because the lower average mechanical aperture. The surface roughness variations provides alterations in the aperture closer to the average aperture compared to the shallow fracture aperture which means that percentually speaking there will be more effect. This is true for both the influences of the initial anisotropy and for the influences of shear length.

When looking at all the  $|-$  shear  $k_x$  data sets we see the maximum permeability is reached when the shear length is equal to the correlation length but also that the maximum permeability is larger the lower the correlation length.

The variations in the permeability in this section are shown to be significant but within one order of magnitude.

## 3.2 Effect of fracture presence in 3D with anisotropic permeability

Before we start complex 3D simulations it is good to test whether the model is working properly and so a simple fracture network is tested. Using the theory we can already make predictions on what kind of results we should get. This simulation will show the significance of fractures and anisotropy in their permeabilities in a 3D grid. Using time of flight calculations the fluid front will be shown moving through the fractures and the semi-permeable rock matrix and heat transport simulations will be done to show the effect of the anisotropic fracture permeability on flow over time using breakthrough curves.

### 3.2.1 3D simple network modelling details

To test the validity of the 3D simulation a simplified scenario is tested. A 3d grid is constructed with the following specifications:

$$x_{\min} = -0.8 \text{ m}$$

$$x_{\max} = 0 \text{ m}$$

$$y_{\min} = -0.3 \text{ m}$$

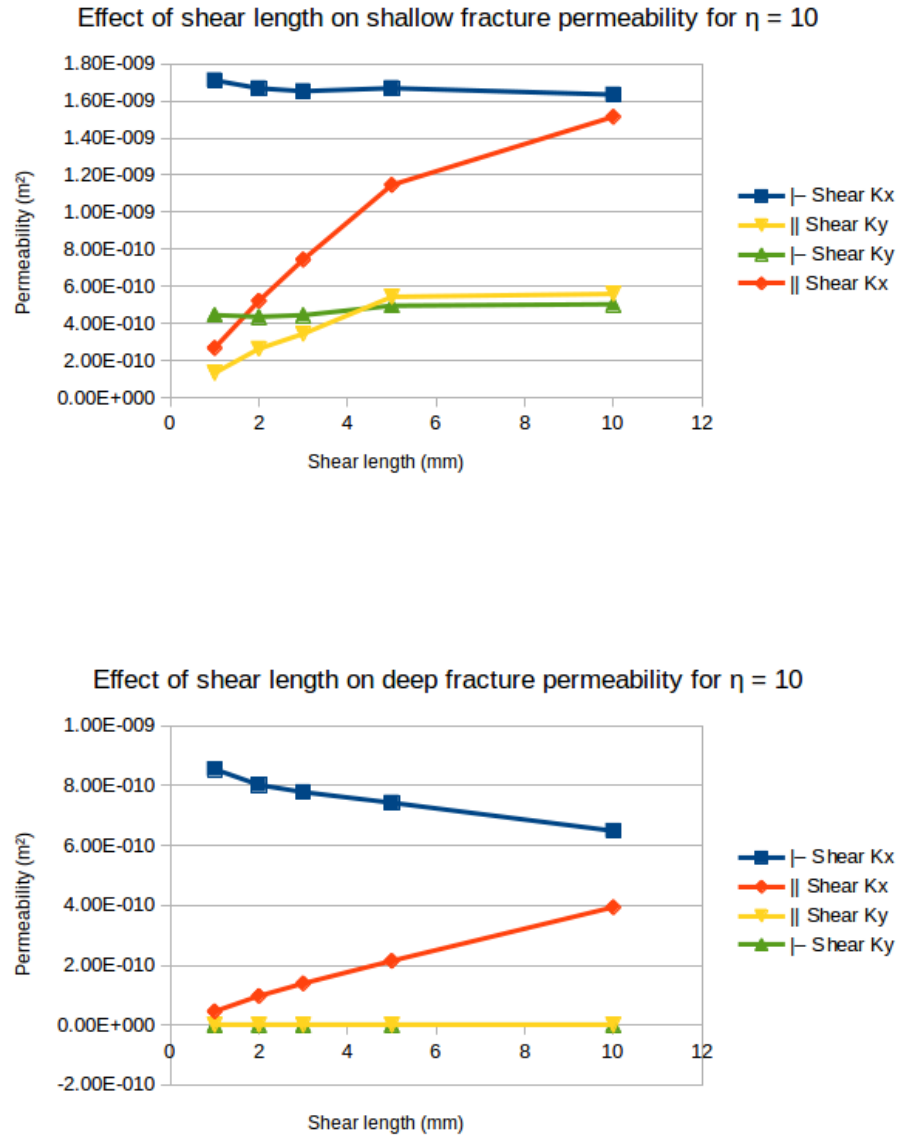


Figure 3.12: Permeability for the fractures with varying shear length and  $\eta = 10$ . In the cases with parallel shear the permeability is shown to increase but in the case with perpendicular shear the permeability in the x-direction is shown to decrease.

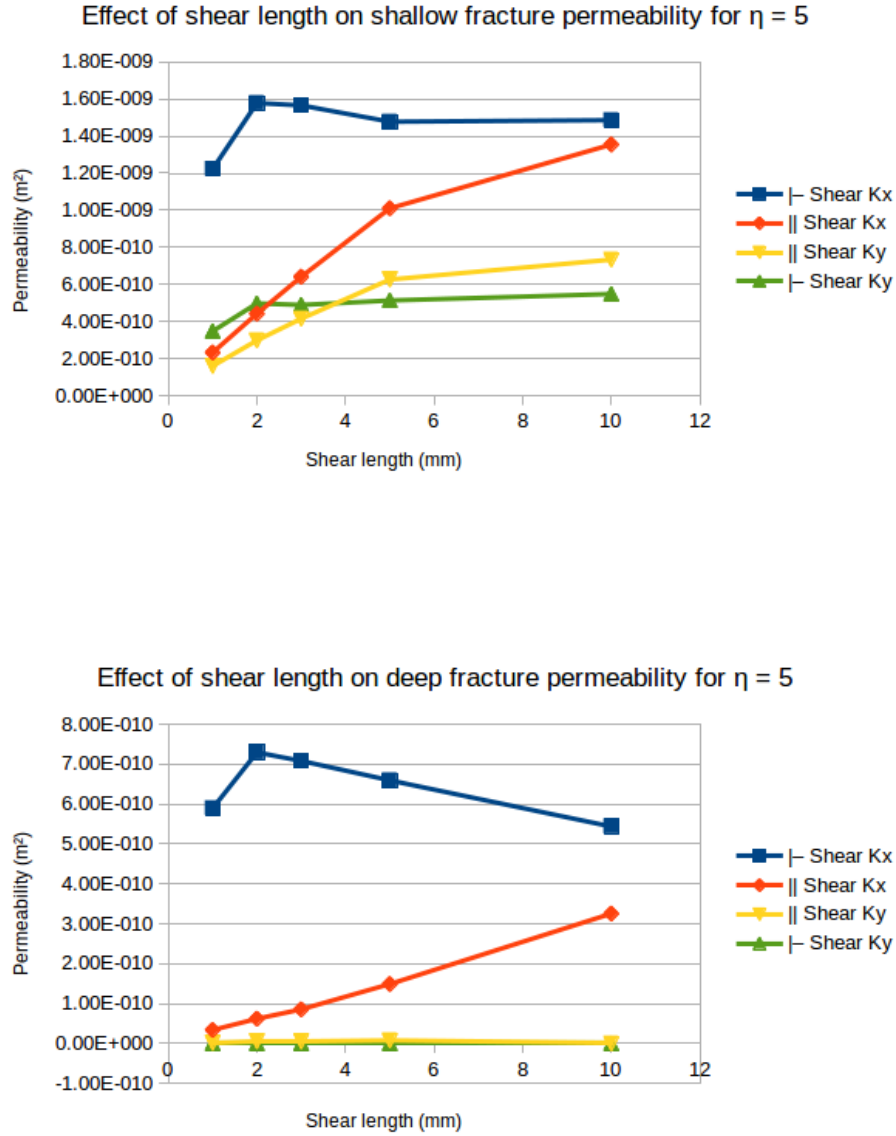


Figure 3.13: Permeability for the fractures with varying shear length and  $\eta = 5$ . In the cases with parallel shear the permeability is shown to increase but in the case with perpendicular shear the permeability in the x-direction is shown to only increase until shear length = 2mm. At this point the shear length is equal to the correlation length and the permeability starts to decrease.

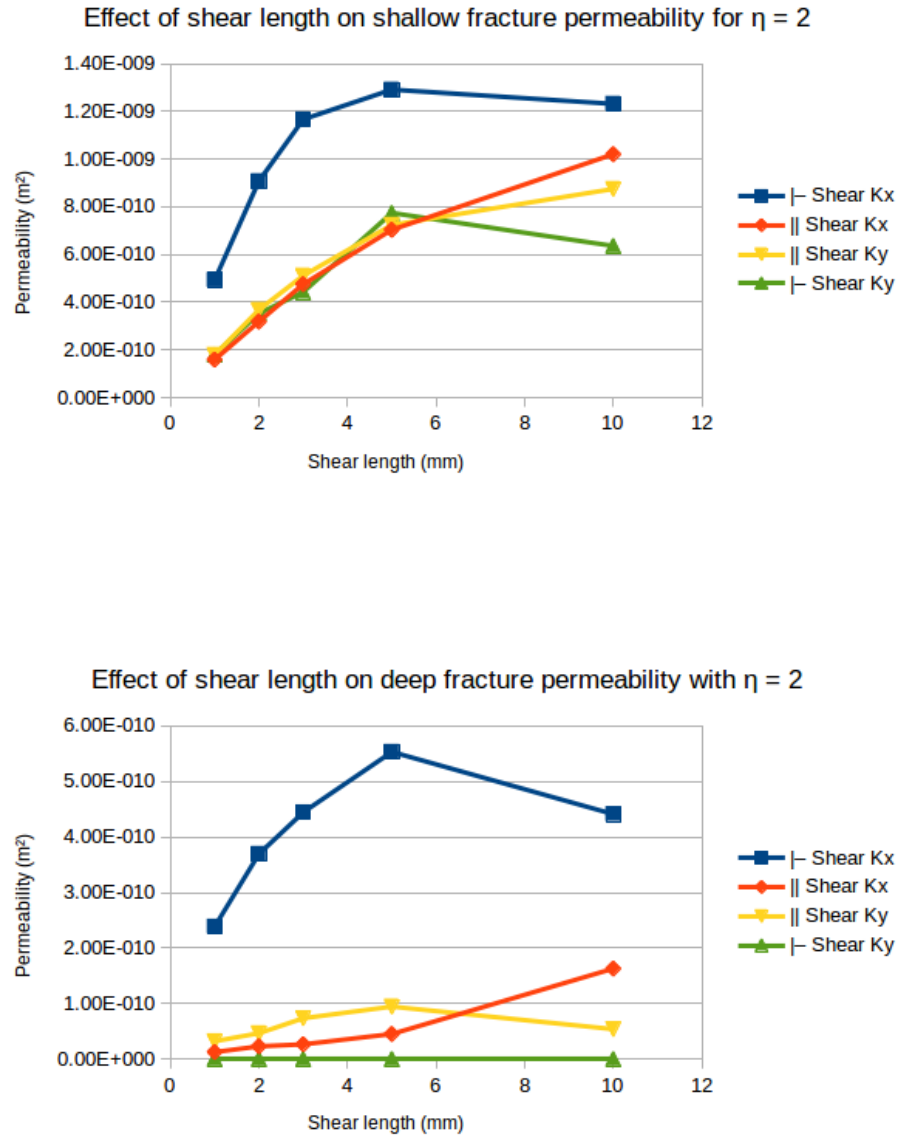


Figure 3.14: Permeability for the fractures with varying shear length and  $\eta = 2$ . In the cases with parallel shear the permeability is shown to increase but in the case with perpendicular shear the permeability in the x-direction is shown to only increase until shear length = 5mm. At this point the shear length is equal to the correlation length and the permeability starts to decrease.



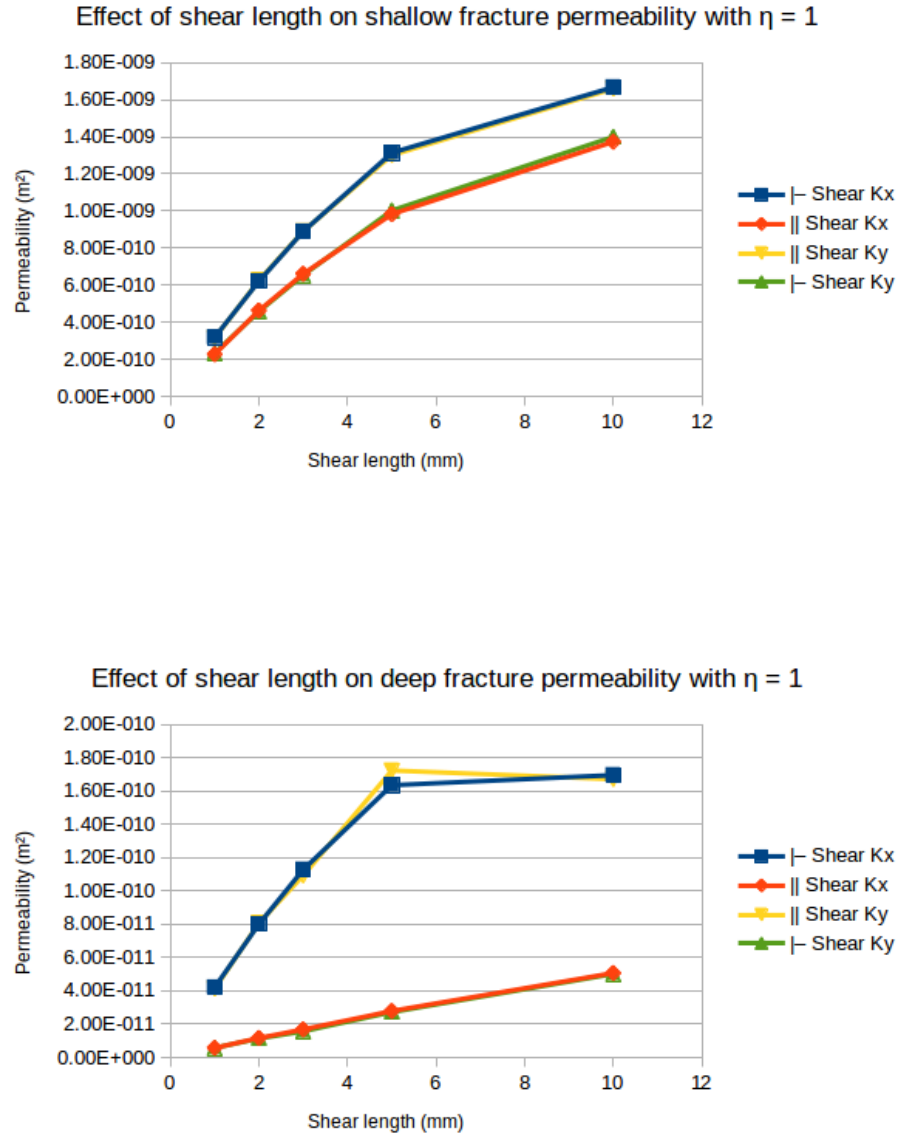


Figure 3.15: Permeability for the fractures with varying shear length and  $\eta = 1$ . In both cases the permeability increases with increasing shear length. Notable here is the differences in permeabilities when perpendicular to the direction of shear and parallel to the direction of shear. Since we started with an isotropic surface all differences originate from the effects of shear.

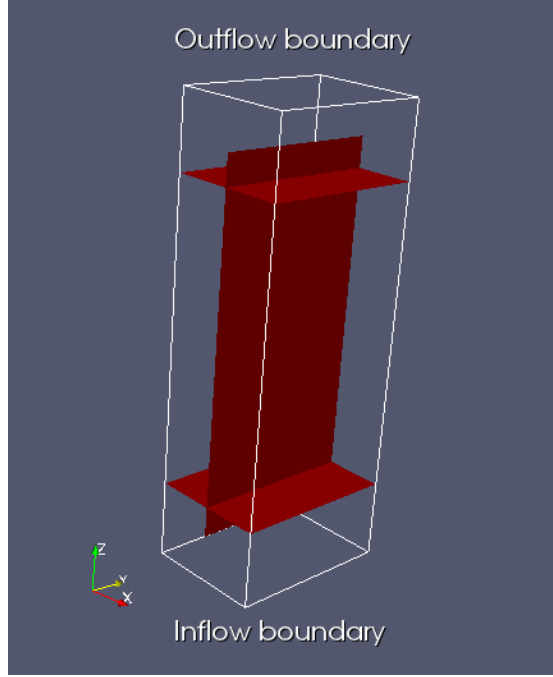


Figure 3.16: The fracture network for the simple network simulations. Two in the x-y plane at height  $z = -0.5$  m and height  $z = -2.5$  m and one in the y-z plane at length  $x = -0.4$  m. The fractures in the x-y plane cross through the model but the fracture in the y-z plane stops 0.3 m before the start and the ending of the grid.

$$\mathbf{ymax} = 0.8 \text{ m}$$

$$\mathbf{zmin} = -3 \text{ m}$$

$$\mathbf{zmax} = 0 \text{ m}$$

In this grid three fractures are defined, shown in Figure 3.16.

These fractures are chosen to show how a pressure front is affected by a permeable fracture. Fracture aperture is set to  $100 \mu\text{m}$ . To test the validity of the 3d simulation the following different anisotropic fracture permeabilities are tested with a constant rock permeability of  $10\mu D$ :

$$\text{Isotropic: } (k_x, k_y, k_z) = (10, 10, 10) \cdot D$$

$$\text{Anisotropic x: } (k_x, k_y, k_z) = (100, 10, 10) \cdot D$$

$$\text{Anisotropic y: } (k_x, k_y, k_z) = (10, 100, 10) \cdot D$$

$$\text{Anisotropic z: } (k_x, k_y, k_z) = (10, 10, 100) \cdot D$$

Anisotropic xy:  $(k_x, k_y, k_z) = (100, 100, 10) \cdot D$

Anisotropic xz:  $(k_x, k_y, k_z) = (100, 10, 100) \cdot D$

Anisotropic yz:  $(k_x, k_y, k_z) = (10, 100, 100) \cdot D$

In addition to these scenarios a simulation is done where the fracture permeability is equal to the matrix permeability. Flow is pressure driven by using boudary conditions. At the face where  $z = -3$  m pressure is set to 100 bar and at the face where  $z = 0$  m pressure is set to 0 bar. All other boudary conditions are no flow. The difference between the higher and lower fracture permeability is set to one order of magnitude as this is the maximum found in the 2D single fracture simulations under equal conditions. The exact permeabilities from the previous simulations vary from 5 Darcy to 1000 Darcy so the values of 10 Darcy and 100 Darcy were chosen since for the purposes of these simulations we're investigating the effects of differences in permeabilities. The dispersive flux is set to 5-10% of the advective flux as this is realistic [18]. The temperature in the model is set to  $T=0$  and the temperature at the inflow boundary is set to  $T=1$ . A dimensionless value is chosen as these simulations focus on the transport and not the intricacies of temperature changes in a rock system.

Flow is solved and the pressure distribution, flux, time-of-flight and temperature over time at the outflow boundary are taken as a result.

### 3.2.2 3D simple network convergence test

When entering the realm of 3D simulations the computational cost versus the amount of detail in the simulation is a consideration that needs to be made. To make sure the results are accurate without having a drastically high computational cost a convergence test is done. The flow and heat transport simulations are done for different grid and fracture resolutions to test which resolution is fine enough for consistent results yet rough enough to obtain resonable computational costs. A total of four simulations per scenario is done with a rough matrix (Mr), a fine matrix (Mf), a rough fracture (Fr) and a fine fracture (Ff) resolution. The breakthrough curves and the boundary fluxes for the different scenarios are taken as results for comparison.

From these graphs it is visible that while differences are visible they are minor. It is therefore decided to continue with the fine matrix rough fracture grid since this is the most refined grid with an acceptable computational cost. A combination of all scenarios in a single graph is shown in Figure 3.32.

### 3.2.3 3D simple network results and discussion

The time of flight per cell of the simulations is shown in Figures 3.25, 3.26, 3.27, 3.28, 3.29, 3.30 and 3.31. Since this is a direct result of the permeability of both the matrix and the fractures clear differences between the different scenarios can be seen.

BC.flux	Ani x	Ani y	Ani z	Ani xy	Ani xz	Ani yz	Iso	No frac
Mr, Fr	2.17E-8	2.42E-8	3.17E-8	2.43E-8	3.19E-8	3.56E-8	2.17E-8	1.90E-8
Mr, Ff	2.24E-8	2.49E-8	3.30E-8	2.49E-8	3.32E-8	3.74E-8	2.24E-8	1.96E-8
Mf, Fr	2.23E-8	2.51E-8	3.36E-8	2.51E-8	3.38E-8	3.81E-8	2.23E-8	1.93E-8
Mf, Ff	2.30E-8	2.55E-8	3.38E-8	2.55E-8	3.40E-8	3.83E-8	2.30E-8	2.02E-8

Table 3.1: The fluxes in  $\text{m}^3/\text{s}$  into the system for each resolution and each scenario. While difference can be seen they amount to no more than 10% between the roughest and the finest grid.

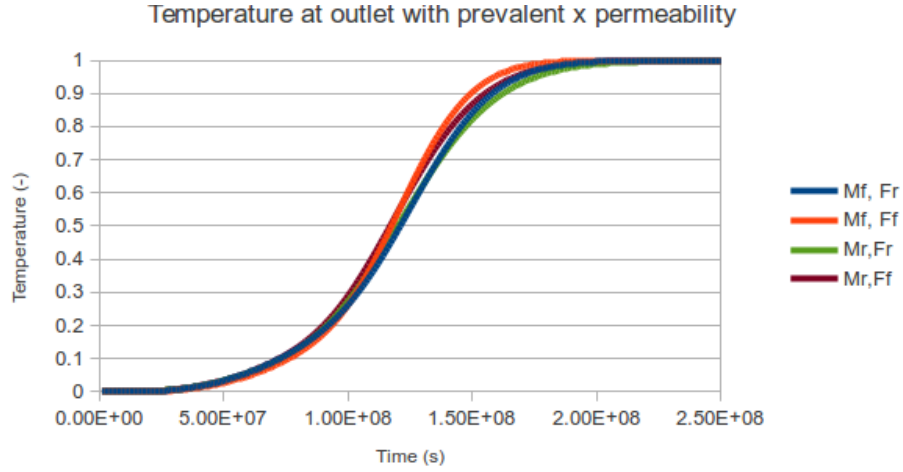


Figure 3.17: Breakthrough curve at the outlet of the model with a matrix permeability of  $10^{-5}D$  and a fracture permeability of  $(k_x, k_y, k_z) = (100, 10, 10) \cdot D$ . While differences are visible between the different resolutions they appear to be minimal.

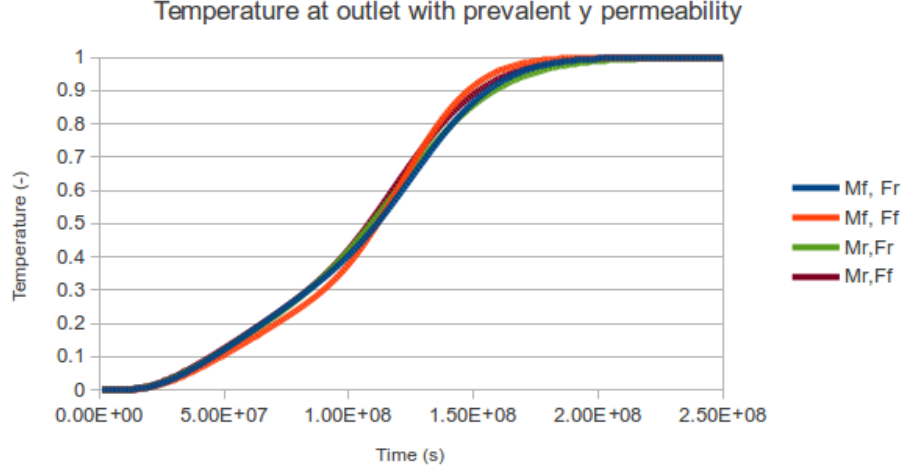


Figure 3.18: Breakthrough curve at the outlet of the model with a matrix permeability of  $10^{-5}D$  and a fracture permeability of  $(k_x, k_y, k_z) = (10, 100, 10) \cdot D$ . While differences are visible between the different resolutions they appear to be minimal.

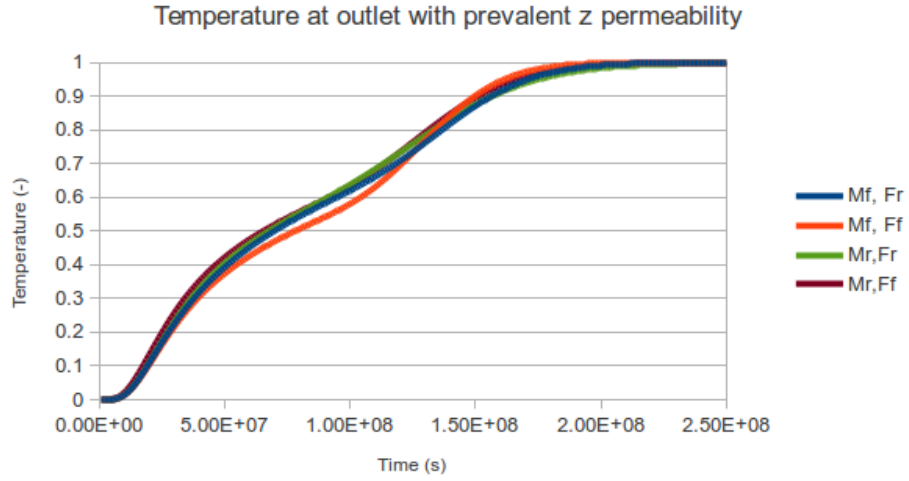


Figure 3.19: Breakthrough curve at the outlet of the model with a matrix permeability of  $10^{-5}D$  and a fracture permeability of  $(k_x, k_y, k_z) = (10, 10, 100) \cdot D$ . While differences are visible between the different resolutions they appear to be minimal.

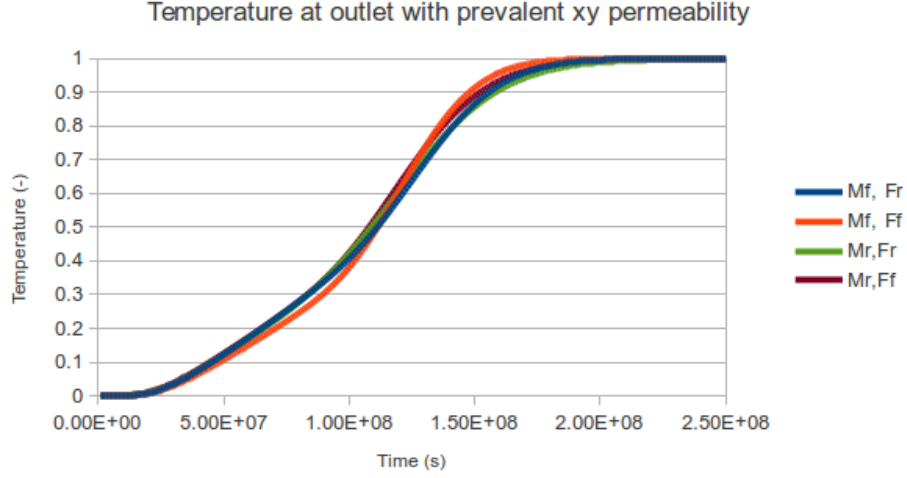


Figure 3.20: Breakthrough curve at the outlet of the model with a matrix permeability of  $10^{-5}D$  and a fracture permeability of  $(k_x, k_y, k_z) = (100, 100, 10) \cdot D$ . While differences are visible between the different resolutions they appear to be minimal.

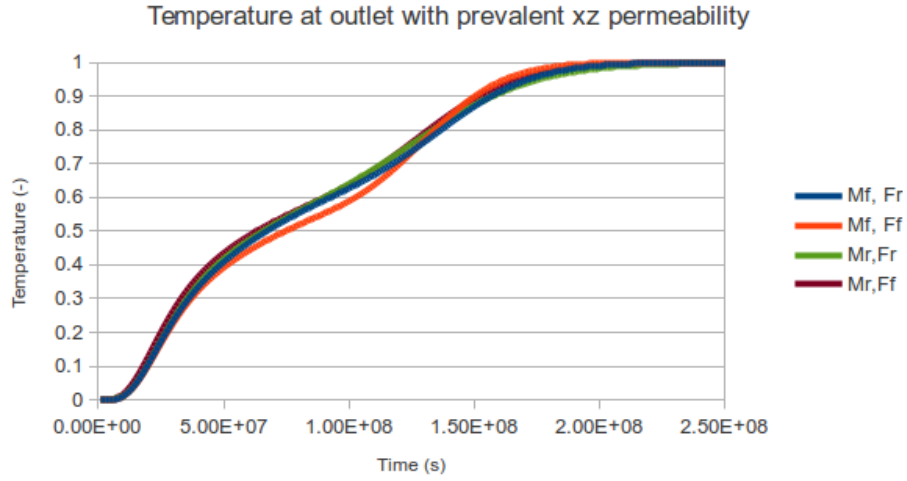


Figure 3.21: Breakthrough curve at the outlet of the model with a matrix permeability of  $10^{-5}D$  and a fracture permeability of  $(k_x, k_y, k_z) = (100, 10, 100) \cdot D$ . While differences are visible between the different resolutions they appear to be minimal.

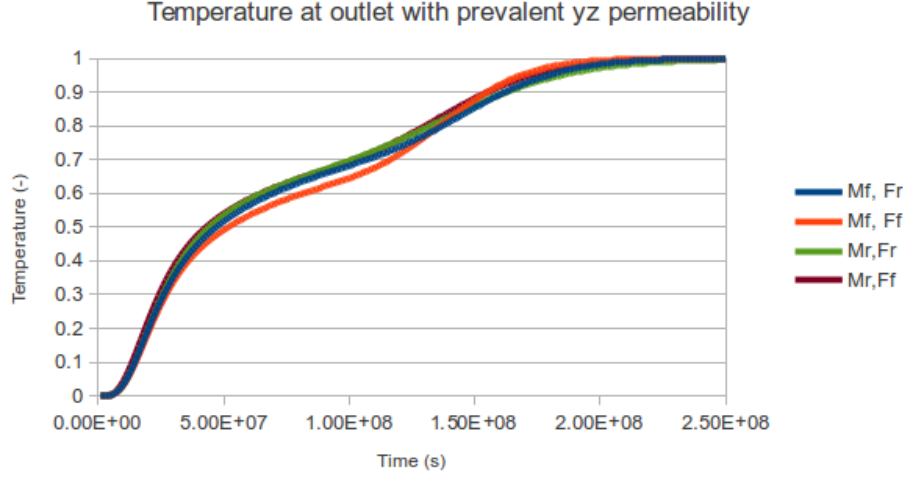


Figure 3.22: Breakthrough curve at the outlet of the model with a matrix permeability of  $10^{-5}D$  and a fracture permeability of  $(k_x, k_y, k_z) = (10, 100, 100) \cdot D$ . While differences are visible between the different resolutions they appear to be minimal.

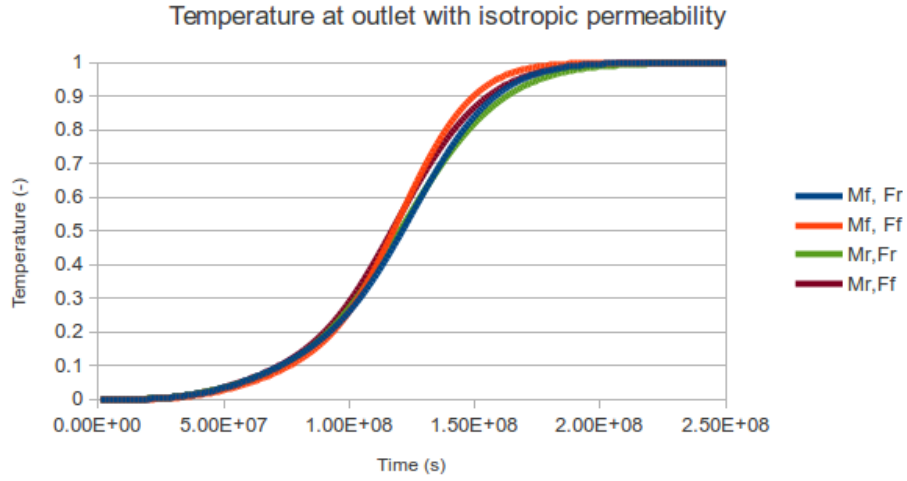


Figure 3.23: Breakthrough curve at the outlet of the model with a matrix permeability of  $10^{-5}D$  and a fracture permeability of  $(k_x, k_y, k_z) = (10, 10, 10) \cdot D$ . While differences are visible between the different resolutions they appear to be minimal.

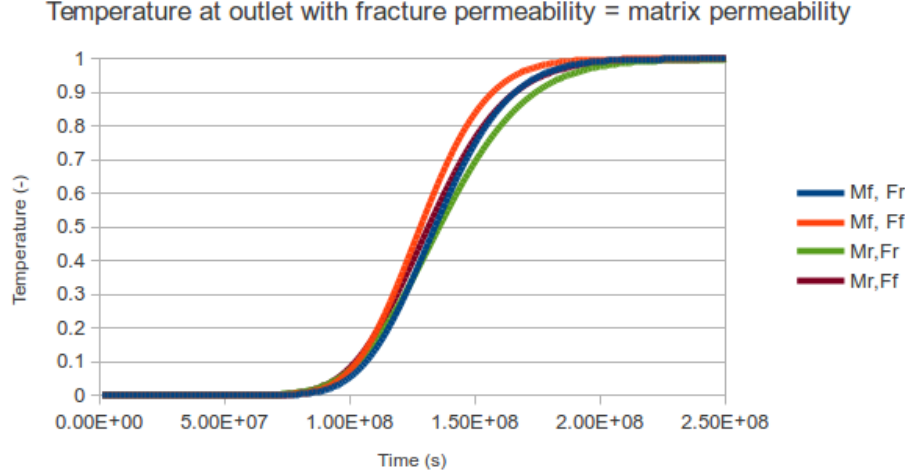


Figure 3.24: Breakthrough curve at the outlet of the model with a matrix permeability of  $10^{-5}D$  and a fracture permeability of  $(k_x, k_y, k_z) = (10^{-5}, 10^{-5}, 10^{-5}) \cdot D$ . While differences are visible between the different resolutions they appear to be minimal.

As expected a clear plume is seen in Figure 3.28 due to the increase permeability in the direction of the pressure difference. The differences between Figures 3.26 and 3.27 are thought to be a result of the error caused by the combination of the two point flux approximation and the unstructured grid. No difference is seen between Figures 3.25 and 3.26.

In the scenarios where we have two prevalent permeability directions not much changes. The results from Figure 3.30 are much like the results from Figure 3.28. This is expected as no difference is seen between Figures 3.25 and 3.26. One important detail is that in the xz scenario where the top horizontal fracture intersects with the vertical fracture the time of flight is lower than in the z scenario. This is the only visible difference caused by an increase in the permeability in the x direction. No differences are visible between Figures 3.29 and 3.27 and only minor differences are visible between Figures 3.31 and 3.28, once again most likely caused by the error originating from using a two point flux approximation with an unstructured grid.

These results are confirmed when looking at the breakthrough curves of the different scenarios in Figure 3.32. The scenarios with a prevalent z permeability show the largest influence and the scenarios with an increase in x permeability show little change.



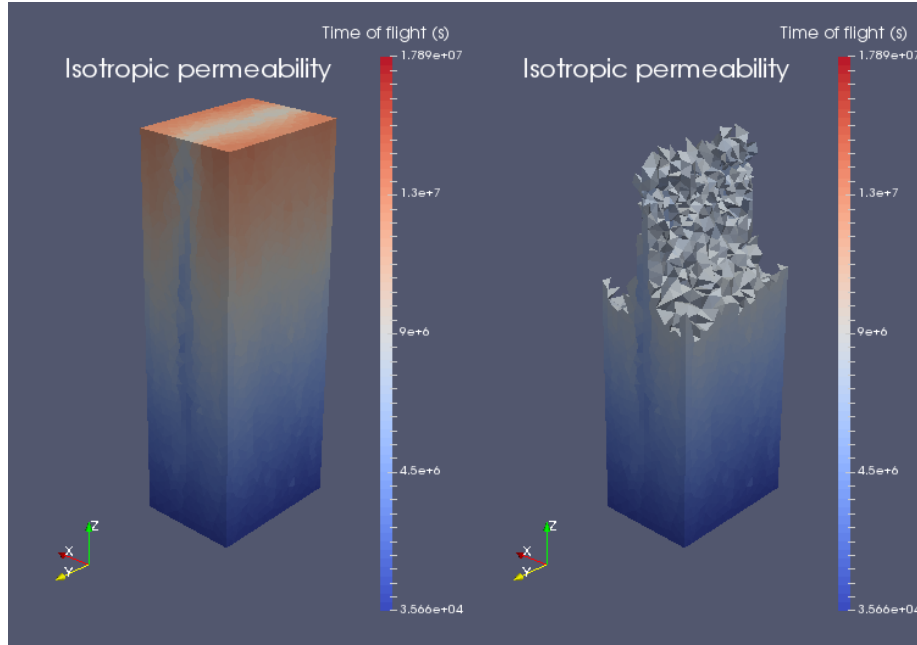


Figure 3.25: Time of flight (s) per cell with a matrix permeability of  $10^{-5}D$  and a fracture permeability of  $(k_x, k_y, k_z) = (10, 10, 10) \cdot D$ . On the left hand side the full grid is shown, on the right hand side only cells with a time of flight of under  $8 \times 10^6$  seconds are shown.

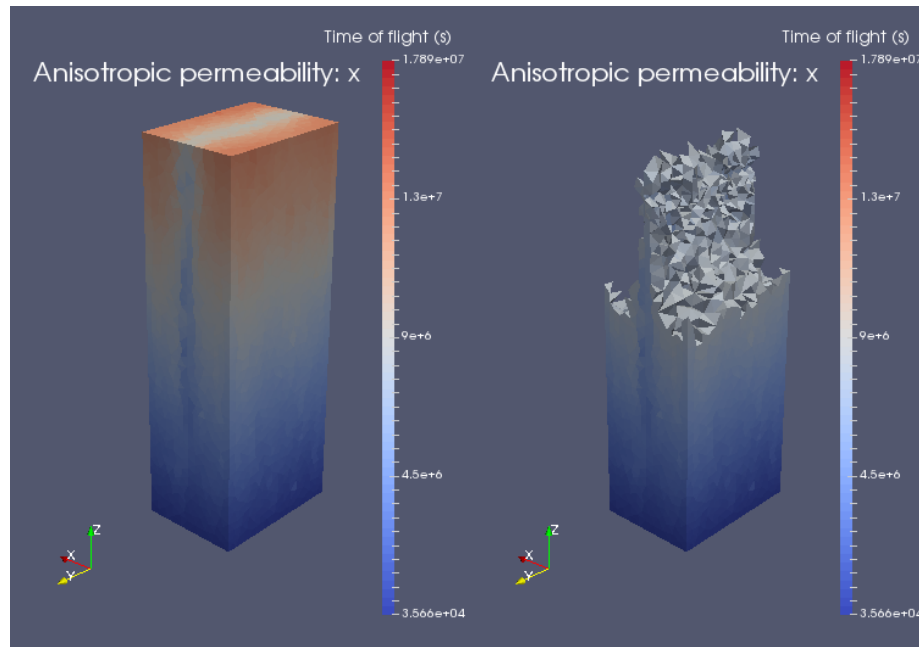


Figure 3.26: Time of flight (s) per cell with a matrix permeability of  $10^{-5}D$  and a fracture permeability of  $(k_x, k_y, k_z) = (100, 10, 10) \cdot D$ . On the left hand side the full grid is shown, on the right hand side only cells with a time of flight of under  $8 \times 10^6$  seconds are shown.

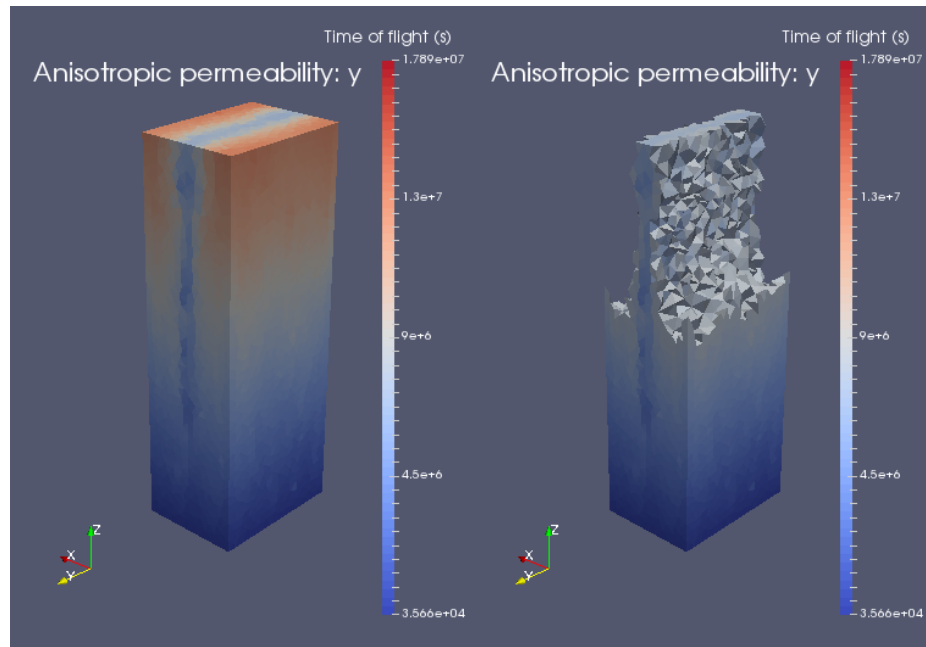


Figure 3.27: Time of flight (s) per cell with a matrix permeability of  $10^{-5}D$  and a fracture permeability of  $(k_x, k_y, k_z) = (10, 100, 10) \cdot D$ . On the left hand side the full grid is shown, on the right hand side only cells with a time of flight of under 8e6 seconds are shown.

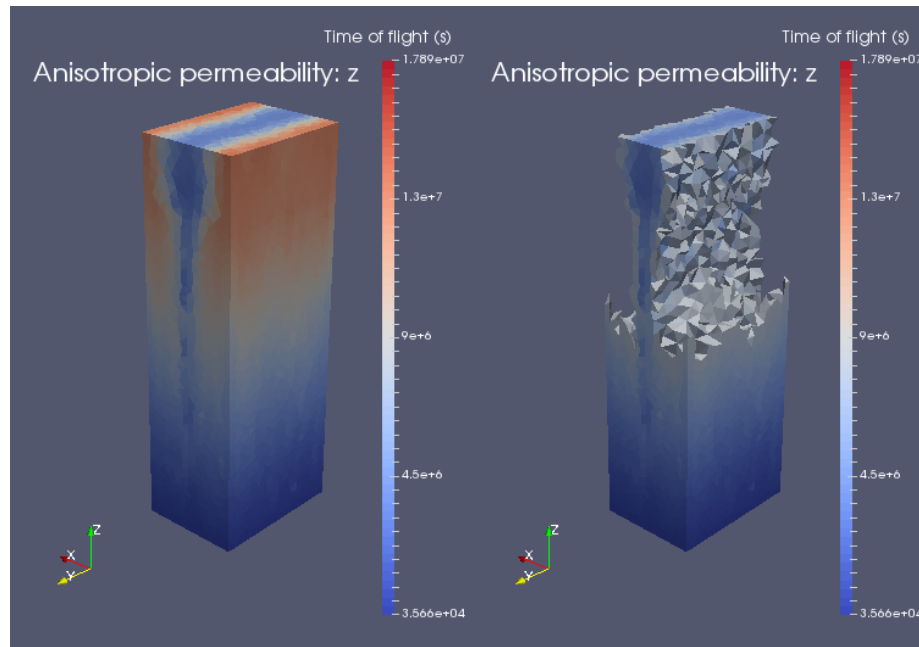


Figure 3.28: Time of flight (s) per cell with a matrix permeability of  $10^{-5}D$  and a fracture permeability of  $(k_x, k_y, k_z) = (10, 10, 100) \cdot D$ . On the left hand side the full grid is shown, on the right hand side only cells with a time of flight of under 8e6 seconds are shown.

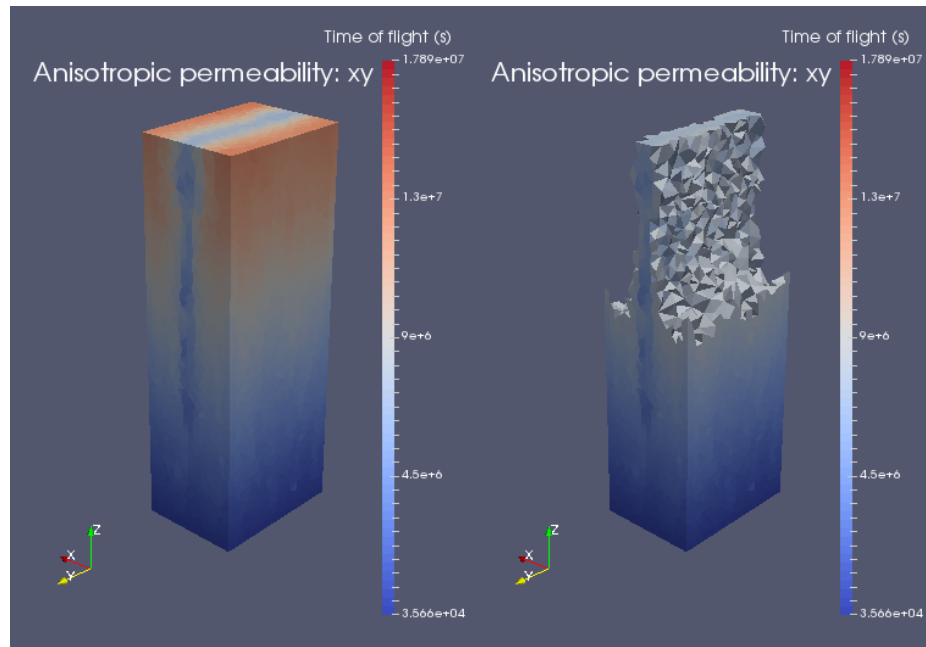


Figure 3.29: Time of flight (s) per cell with a matrix permeability of  $10^{-5}D$  and a fracture permeability of  $(k_x, k_y, k_z) = (100, 100, 10) \cdot D$ . On the left hand side the full grid is shown, on the right hand side only cells with a time of flight of under  $8 \times 10^6$  seconds are shown.

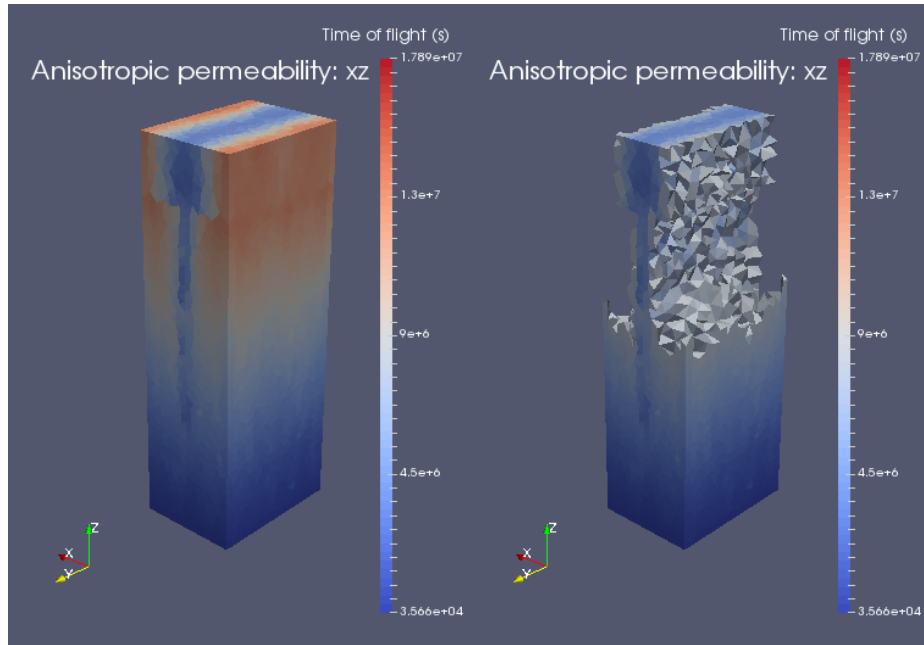


Figure 3.30: Time of flight (s) per cell with a matrix permeability of  $10^{-5}D$  and a fracture permeability of  $(k_x, k_y, k_z) = (100, 10, 100) \cdot D$ . On the left hand side the full grid is shown, on the right hand side only cells with a time of flight of under  $8e6$  seconds are shown.

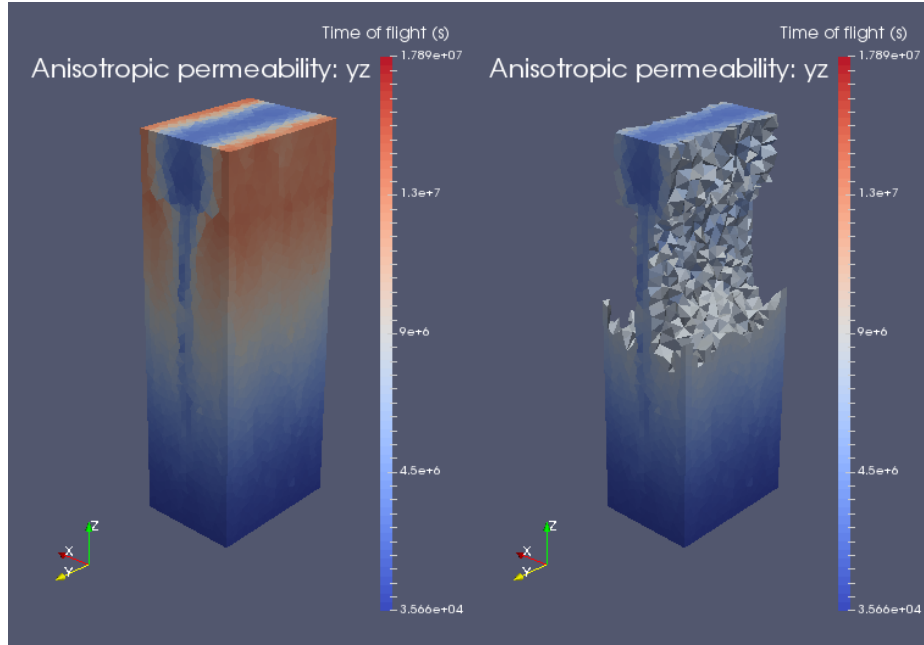


Figure 3.31: Time of flight (s) per cell with a matrix permeability of  $10^{-5}D$  and a fracture permeability of  $(k_x, k_y, k_z) = (10, 100, 100) \cdot D$ . On the left hand side the full grid is shown, on the right hand side only cells with a time of flight of under 8e6 seconds are shown.

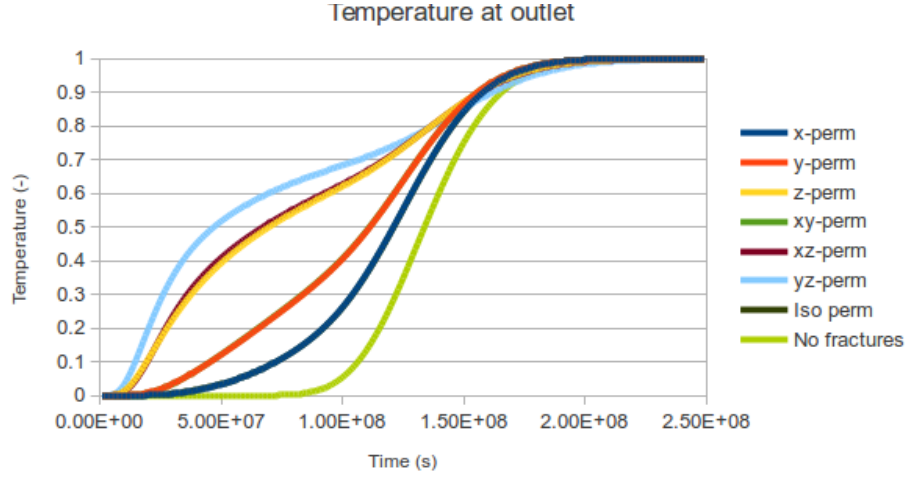


Figure 3.32: The temperature at the outflow boundary over time for every scenario. The time here is significantly higher than the time calculated in the time of flight calculations because the time of flight shows at what point in time the particles from the inflow boundary reach the cell while the temperature shows when the volume of the cell is completely replaced with particles from the inflow boundary.

### 3.3 Effect of stress on a fracture network with anisotropic permeability

Applying the results from the previous simulations we will now simulate a complex fracture network with an anisotropic permeability determined by an assigned confining pressure, which translates into different effective normal stress on different sets of fractures. By using wells the effects of the anisotropic permeability should be more visible then when using boundary conditions. To further enhance this effect the fractures are designed in a way that no direct path between the wells exists. As output we will take the breakthrough curve at the outflow well and we will also show the time of flight of the cells in the sytem.

#### 3.3.1 3D complex fracture network modelling details

A 3D grid is constructed with the following specifications:

$$x_{\min} = 0 \text{ m}$$

$$x_{\max} = 10 \text{ m}$$

$$y_{\min} = 0 \text{ m}$$

$$y_{\max} = 10 \text{ m}$$



**zmin** = 0 m

**zmax** = 10 m

In this grid a total of 32 fractures are defined. First we have a total of eleven major fractures spanning the grid. They are all parallel to each other, spaced out one meter in between, and tilted  $\frac{1}{8}\pi$  radians with respect to the x-axis. The fractures are cut short when intersecting with the edges of the grid. These major fractures are shown in Figure 3.33.

Connecting these fractures are the 21 smaller fractures. These minor fractures connect from one fracture to the next and are tilted  $\frac{1}{4}\pi$  radians with respect to the y-axis. They extend 0.2m beyond each fracture because the gridding code is vulnerable to error when modelling touching fractures. The grid with both the major and minor fractures and the locations of the wells is shown in Figures 3.34 and 3.35.

Three scenario's are tested. One where the fracture permeability is small and isotropic in all directions, one where the confining pressure is perpendicular to the major fractures resulting in a larger permeability in the minor fractures and one where the confining pressure is perpendicular to the minor fractures resulting in a larger permeability in the major fractures. The isotropic scenario is chosen to have a small permeability to show the effects of increasing permeability in fractures as this is the point of inducing shear through hydrodynamic stimulation of reservoirs. In addition, both the major and minor fractures have an anisotropic permeability distribution. This is to represent an already stimulated reservoir where the effects of the initial fracture surface wall anisotropy and induced shear have already altered the permeability. For the major fractures the  $k_y = 10k_x$  to indicate anisotropy in the  $y$ -direction with shear in the  $x$ -direction and for the minor fractures the  $k_x = 10k_y$ . The matrix permeability is kept constant at  $1\mu D$ . In total the assigned permeabilities are listed as

Isotropic:  $(k_x, k_y, k_z)_{major} = (10, 10, 10) \cdot D$

$$(k_x, k_y, k_z)_{minor} = (10, 10, 10) \cdot D$$

Confining pressure on major fractures:

$$(k_x, k_y, k_z)_{major} = (10, 100, 10) \cdot D$$

$$(k_x, k_y, k_z)_{minor} = (100, 10, 1000) \cdot D$$

Confining pressure on minor fractures:

$$(k_x, k_y, k_z)_{major} = (100, 1000, 10) \cdot D$$

$$(k_x, k_y, k_z)_{minor} = (100, 10, 10) \cdot D$$

Fracture aperture is set to  $100\mu m$ . Flow is pressure driven, the injection well is set to 100 bar and the extraction well is set to 0 bar. All boundary conditions are no-flow. The temperature in the model is set to  $T=0$  and the temperature at the injection well is set to  $T=1$ . The dispersive flux is set to 5-10% of the advective flux.

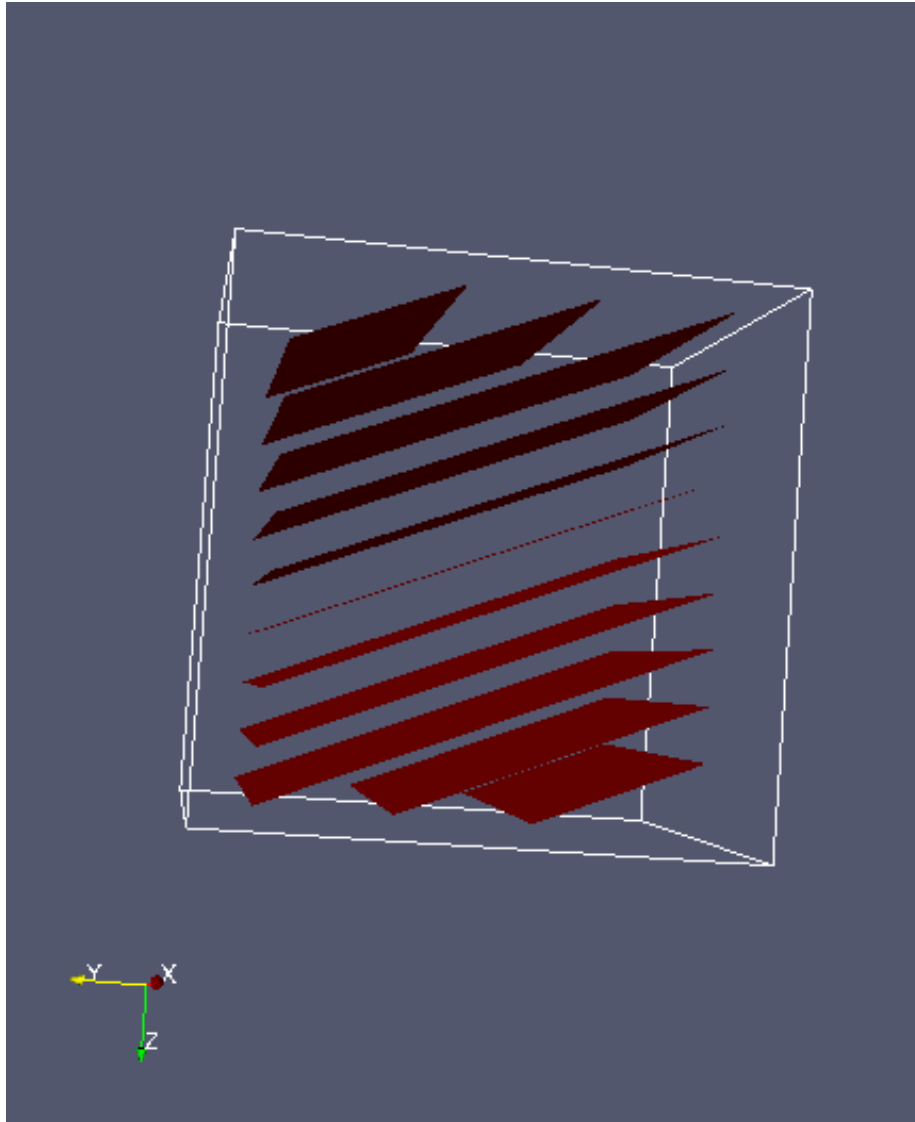


Figure 3.33: The eleven major fractures in the complex grid. All are parallel and 1m apart. The top and bottom two are cut to fit in the grid.

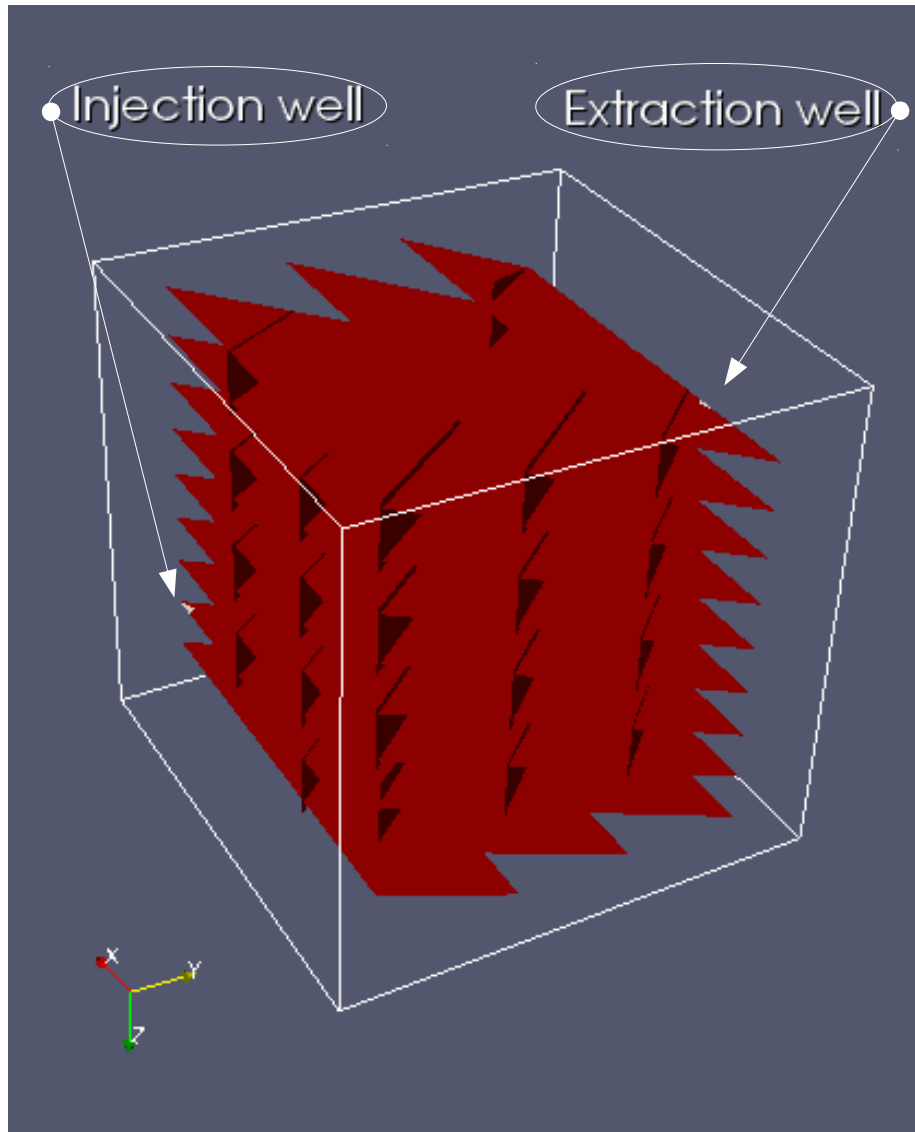


Figure 3.34: The fracture network for the complex simulations. The injection and extraction well locations are shown.

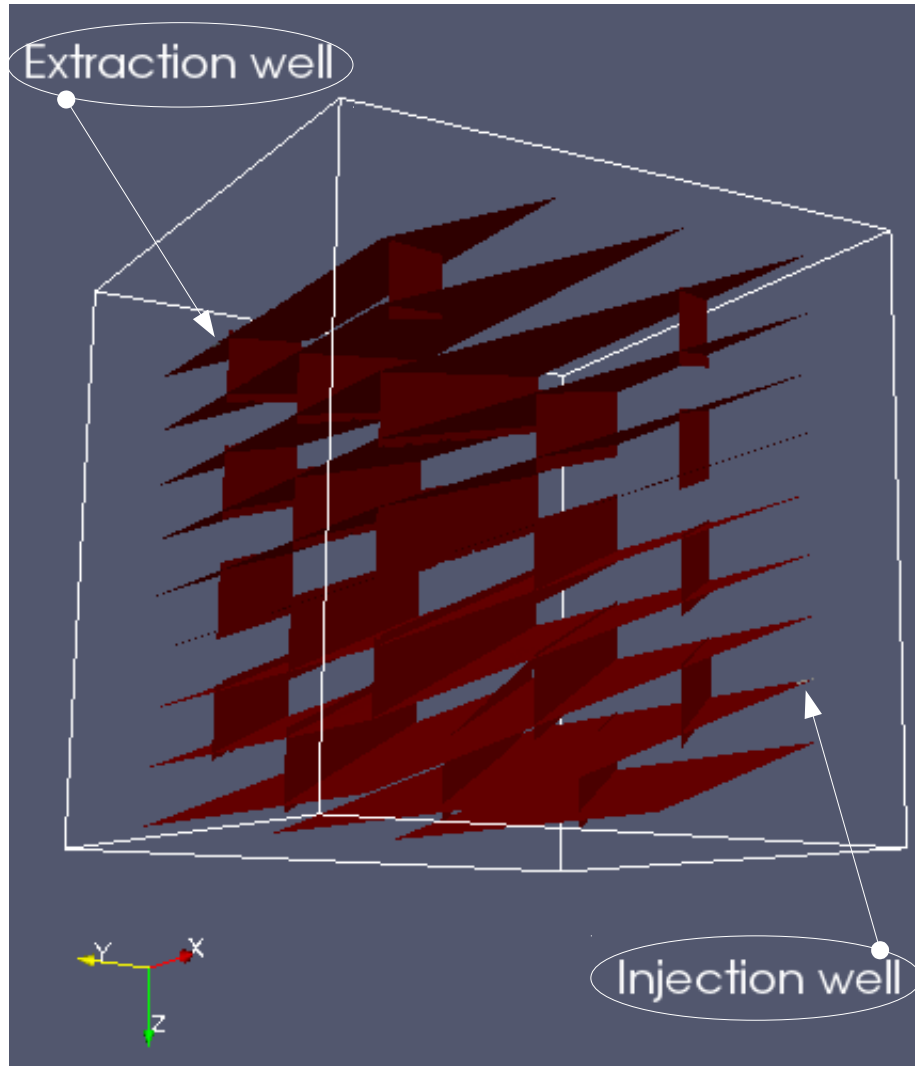


Figure 3.35: The fracture network for the complex simulations from a different angle. The injection and extraction well locations are shown.

### 3.3.2 3D complex fracture network results and discussion

The time of flight in the fractures of the grid is shown in Figures 3.36, 3.37, 3.38, 3.39, 3.40 and 3.41. For every scenario two figures are shown, in the first time of flight is scaled to 1e9s and in the second time of flight is scaled to 5e9s.

Between the three different scenario's clear differences can be seen. The isotropic case shows the least distance traveled for the specific time of flights. This is because the permeability only increases for the other scenarios so this scenario can function as a baseline and will show the effects of increasing different parts of the permeability vectors of the system. In fact, when looking at Figures 3.36 and 3.37 we can see that unconnected parts of fractures are shown for the specified time of flights. This indicates that a large part of the fluid transport is through the matrix between the fractures. The scenario with the confining pressure on the minor fractures shows the largest distance covered by the fluid for the specified time of flight. This is expected since the major fractures are the largest and thus will have the most impact on the fluid flow. In addition, when the fluid easily spreads of the major fractures it will have more minor fractures available for the fluid transport, which effectively increases the permeability. When comparing Figures 3.38 and 3.39 a large difference in the reached area can be seen. Due to the confining pressure on the major fractures the fluid slowly spreads over these fractures but once the minor fractures are reached the fluid easily flows to the next major fracture, indicated by the similarities in the time of flight at the bottom and the top of the minor fractures.

In addition to the time of flight the temperature at the extraction well is calculated and for the three different scenarios shown in Figures 3.42, 3.43 and 3.44. A combination of the three graphs is shown in Figure 3.45.

As would be expected the scenario with the confining pressure on the minor fractures shows the fastest increase in temperature, followed by the scenario with the confining pressure on the major fractures and ended by the scenario with an isotropic permeability. When looking at the individual graphs it is noticeable that in the scenario with confining pressure on the major fractures the increase in extraction temperature appears to start relatively earlier than in the other scenarios, resulting in a graph that's more spread out. The graphs describing the scenarios with isotropic permeability and with confining pressure on the minor fractures look very similar. This implies that a large factor in the form the graph takes is the shape of the fracture network when working with wells.

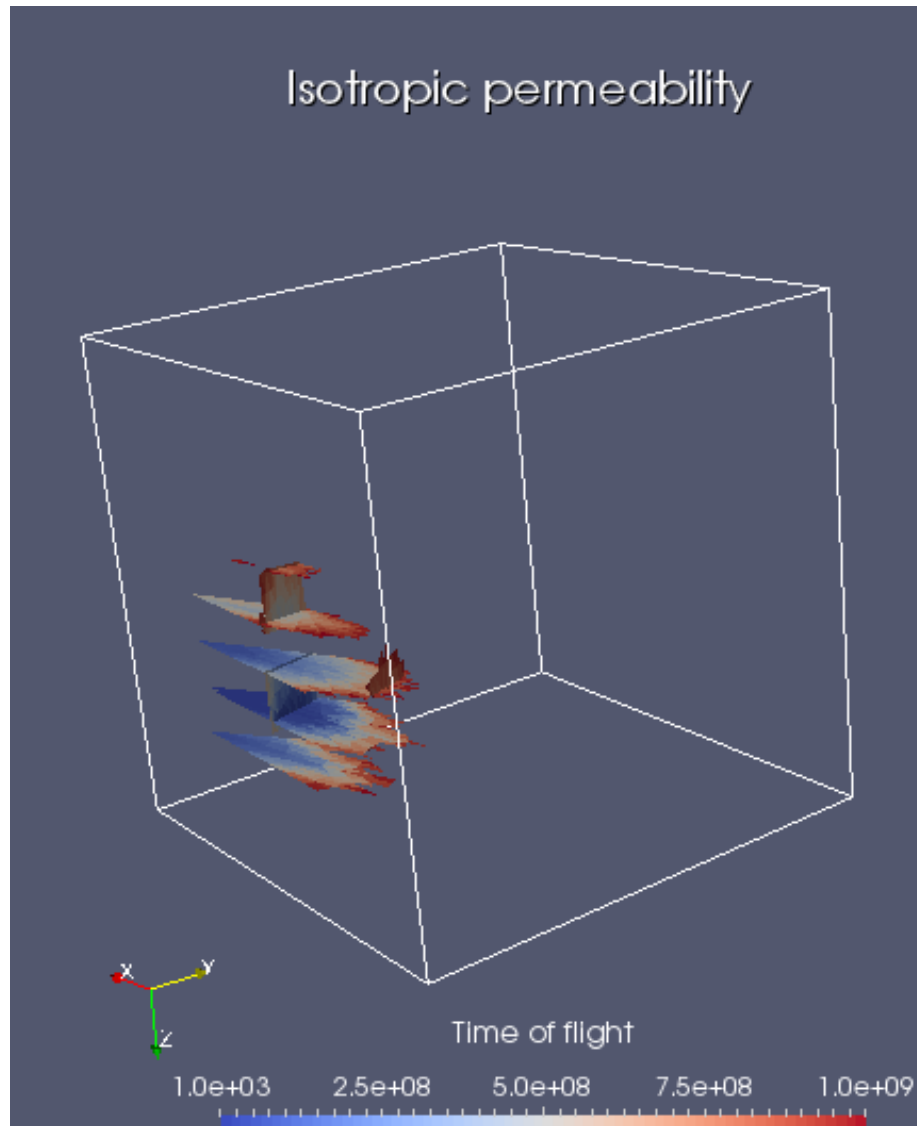


Figure 3.36: The time of flight up to  $1e9$ s of the fracture cells for the scenario with isotropic permeability.

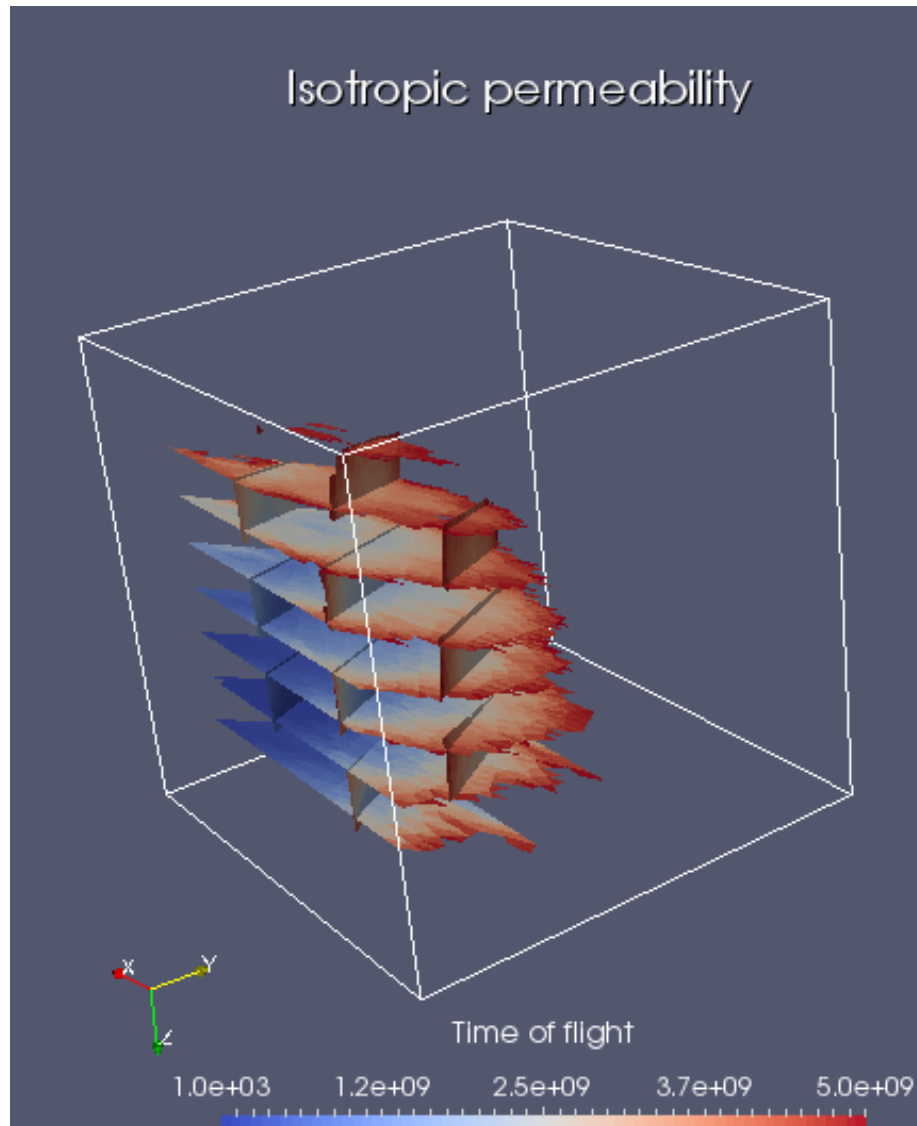


Figure 3.37: The time of flight up to 5e9s of the fracture cells for the scenario with isotropic permeability.

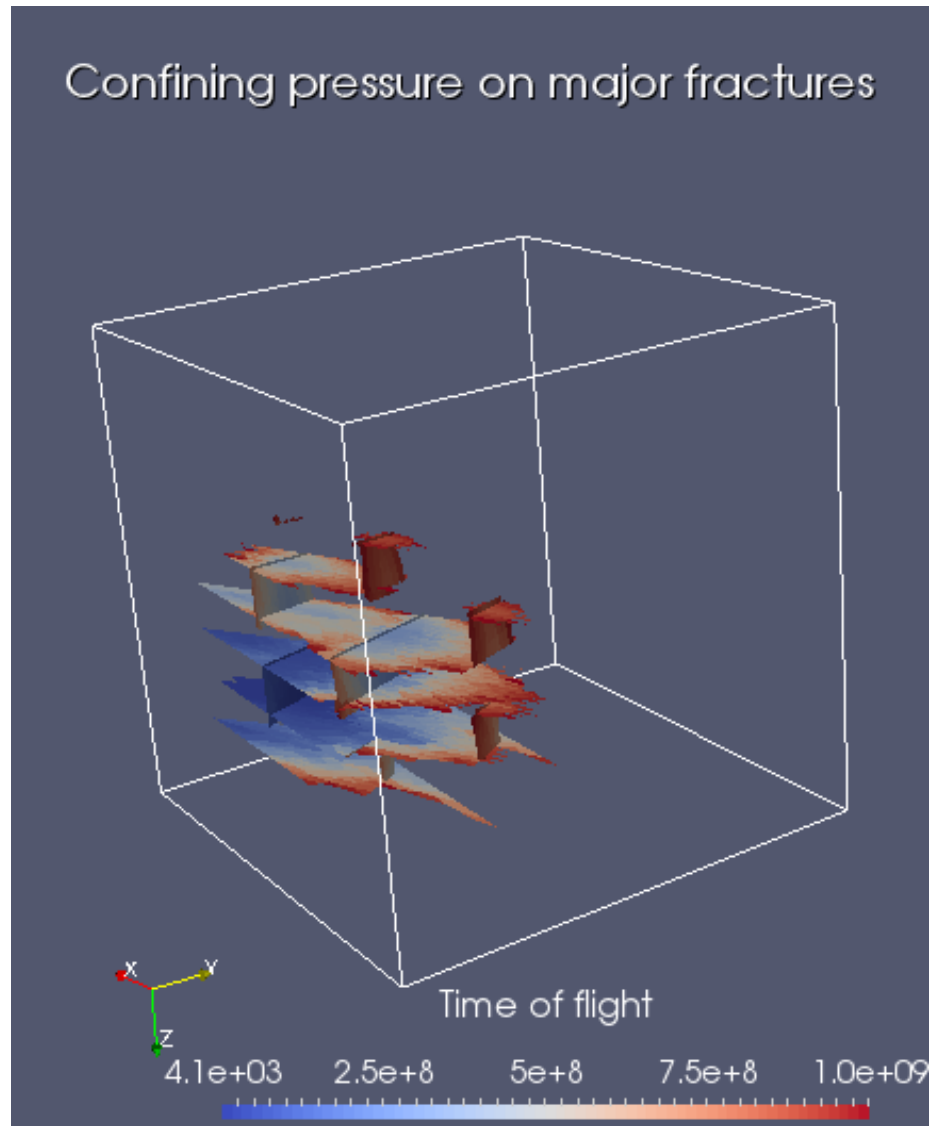


Figure 3.38: The time of flight up to  $1\text{e}9\text{s}$  of the fracture cells for the scenario with confining pressure on the major fractures.



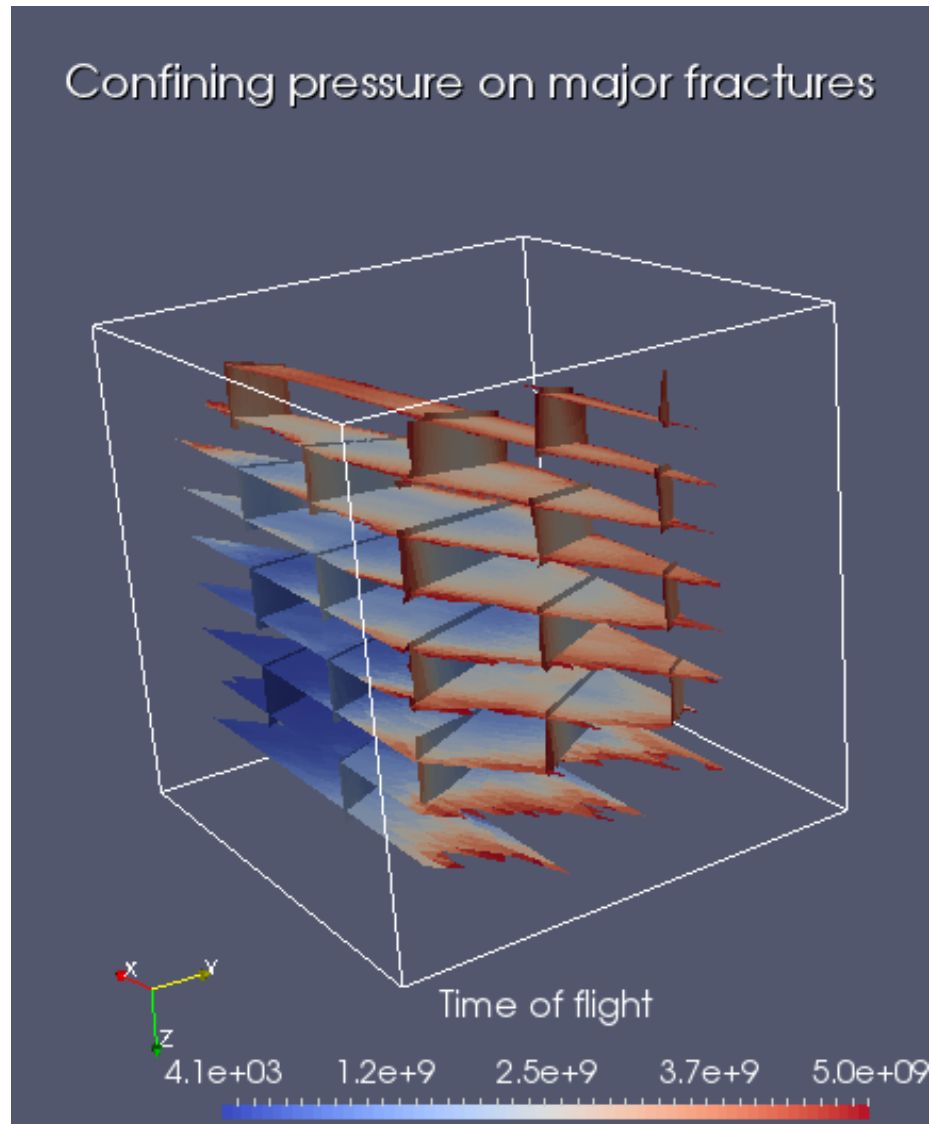


Figure 3.39: The time of flight up to  $5e9$ s of the fracture cells for the scenario with confining pressure on the major fractures.

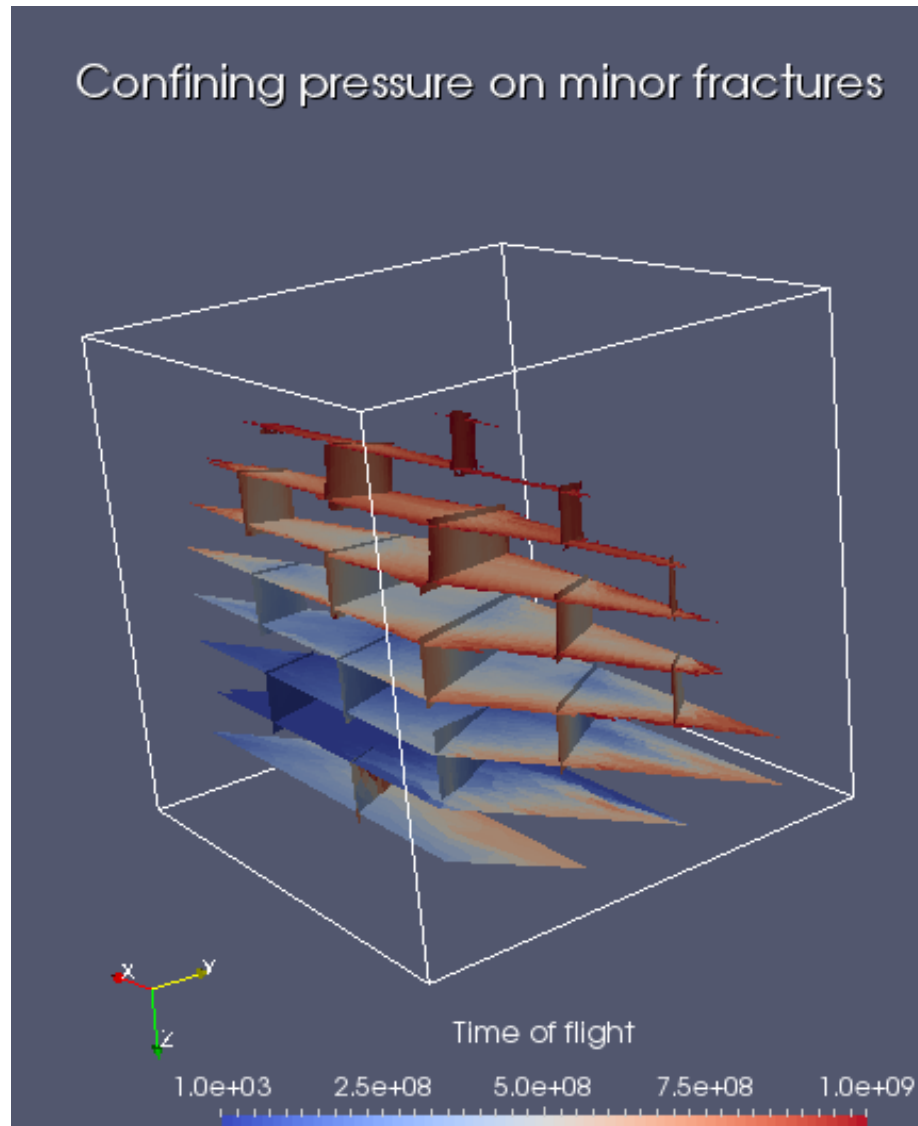


Figure 3.40: The time of flight up to 1e9s of the fracture cells for the scenario with confining pressure on the minor fractures.

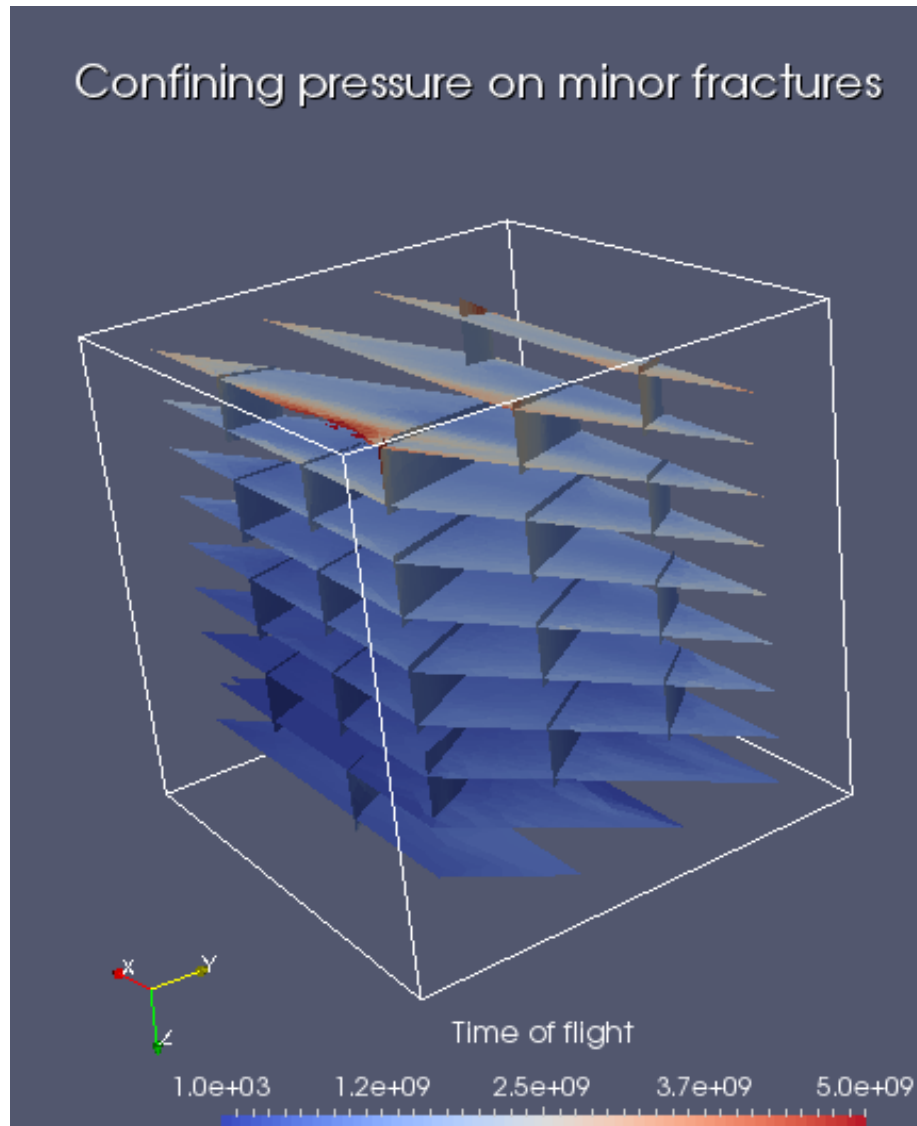


Figure 3.41: The time of flight up to 5e9s of the fracture cells for the scenario with confining pressure on the minor fractures.

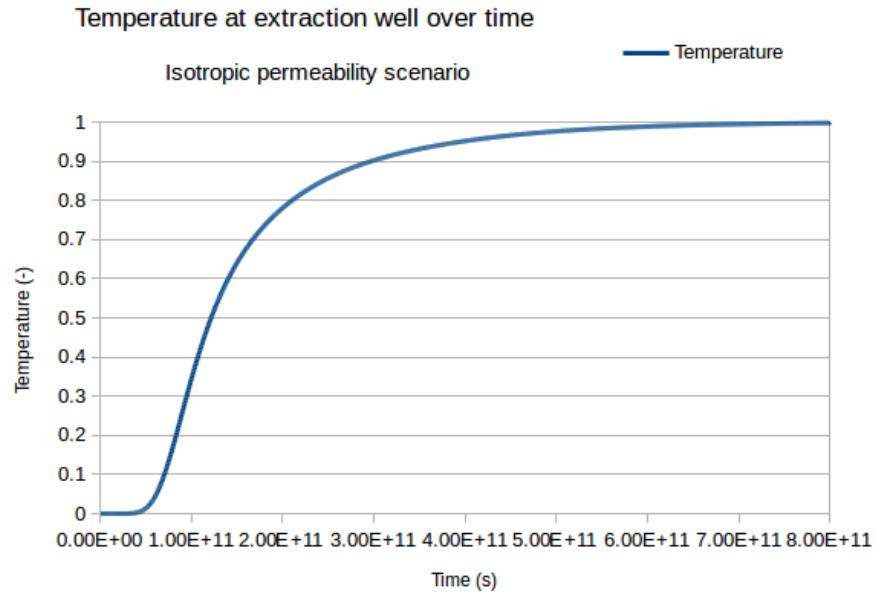


Figure 3.42: The normalized temperature at the extraction well for the scenario with isotropic permeability. Not that the x-axis is set to different times than for figures 3.43 and 3.44.

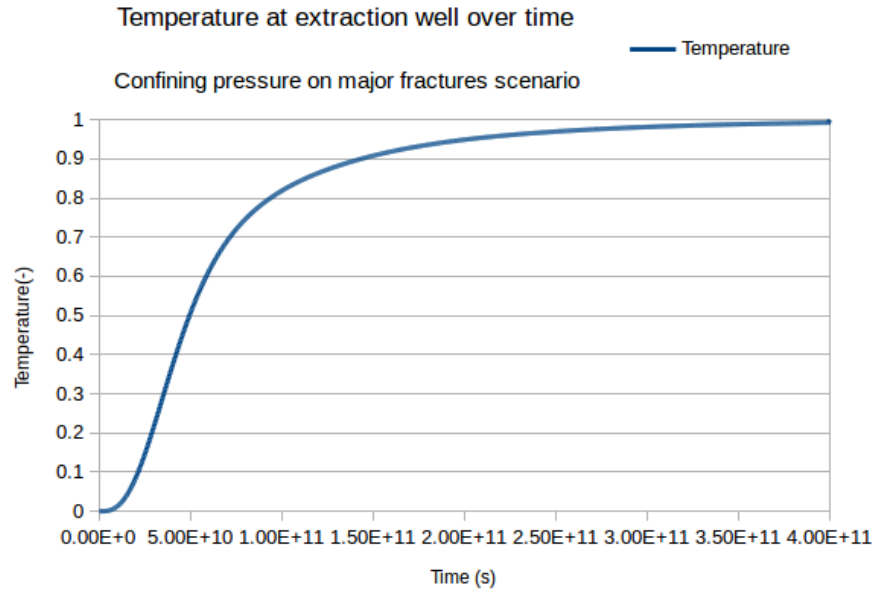


Figure 3.43: The normalized temperature at the extraction well for the scenario with confining pressure on the major fractures. Note that the x-axis is set to different times than for figures 3.42 and 3.44.

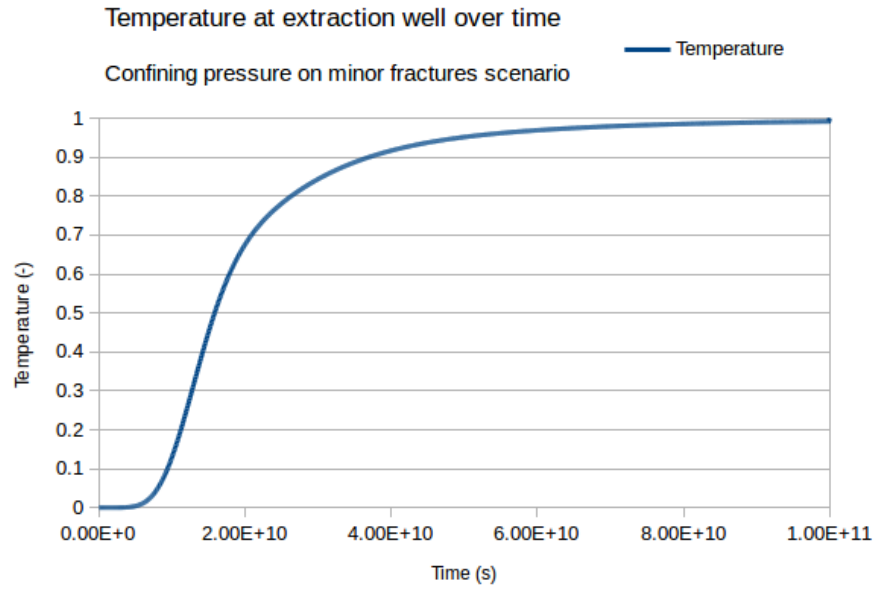


Figure 3.44: The normalized temperature at the extraction well for the scenario with confining pressure on the minor fractures. Note that the x-axis is set to different times than for figures 3.42 and 3.43.

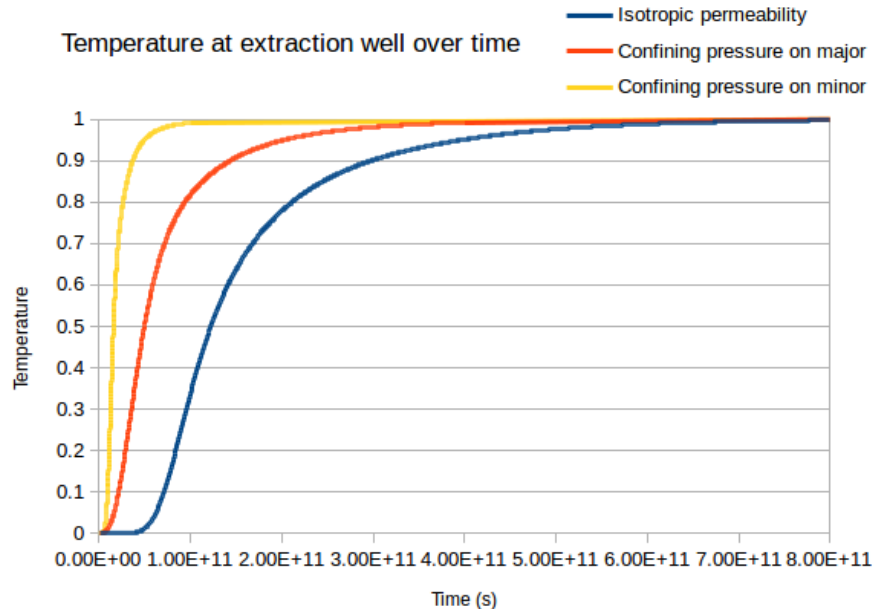


Figure 3.45: The normalized temperature at the extraction well for every scenario.

## Chapter 4

# Conclusions

The initial anisotropy of the fracture surface wall roughness can determine whether a fracture becomes blocking or highly conductive.

Permeability in a single fracture is largest perpendicular to the direction of shear due to the opening of the fracture. When the channels formed by anisotropic fracture surface wall roughness are in the direction of flow this difference can reach one order of magnitude. When the anisotropy is unfavorable shearing perpendicular to the direction of flow increases the permeability and can prevent the creation of blocking fractures. Even when starting with an isotropic fracture surface wall roughness shear creates anisotropy in the permeability of the fracture.

The permeability of the fracture reaches a maximum when the shear length is equal to the correlation length of the fracture surface wall roughness after which it starts to drop again.

While fracture driven flow appears to determine the time required for the injected fluid to reach the extraction point, from the heat simulations it is visible that the smaller fractures that make up the matrix in the simulations is still significant for thermal transport.

The order of magnitude difference in permeability after shear due to the initial fracture wall anisotropy can determine whether fluid is transported mainly through the fracture or through the matrix and could therefore significantly improve volumetric flow through the reservoir.

# Bibliography

- [1] A. Baghbanan and L. Jing. Stress effects on permeability in a fractured rock mass with correlated fracture length and aperture. *International Journal of Rock Mechanics & Mining Sciences*, 45:1320–1334, 2008.
- [2] M. Karimi-Fard, L.J. Durlofsky and K. Aziz. An efficient discrete fracture model applicable for general purpose reservoir simulators. In *SPE Reservoir Simulation Symposium*. Society of Petroleum Engineers, 2003.
- [3] C. Klimczak et al. Cubic law with aperture-length correlation: implications for network scale fluid flow. *Hydrogeology Journal*, 18(4):851–862, 2010.
- [4] M.K. Hubbert et al. *Darcy’s law and the field equations of the flow of underground fluids*. Shell Development Company, Exploration and Production Research Division, 1956.
- [5] W.C. Burton et al. Influence of fracture anisotropy on ground water ages and chemistry, valley and ridge province, pennsylvania. *Ground Water*, 40(3):242–257, 2002.
- [6] I.W.D. Yeo, M.H. De Freitas and R.W. Zimmerman. Effect of shear displacement on the aperture and permeability of a rock fracture. *International Journal of Rock Mechanics and Mining Sciences*, 35.8:1051–1070, 1998.
- [7] C. Geuzaine and J.F. Remacle. Gmsh: A 3-d finite element mesh generator with built-in pre-and post-processing facilities. *International Journal for Numerical Methods in Engineering*, 79(11):1309–1331, 2009.
- [8] N.R. Goodman. Statistical analysis based on a certain multivariate complex gaussian distribution (an introduction). *The Annals of Mathematical Statistics*, 34(1):152–177, 1963.
- [9] E. Hakami and E. Larsson. Aperture measurements and flow experiments on a single natural fracture. *International Journal of Rock Mechanics and Mining Sciences & Geomechanics*, 33(4), 1996.
- [10] J. Ahrens, B. Geveci, C. Law, C.D. Hansen and C.R. Johnson. 36-paraview: An end-user tool for large-data visualization. *The Visualization Handbook*, page 717, 2005.

- [11] K. Nemoto, N. Watanabe, N. Hirano and N. Tsuchiya. Direct measurement of contact area and stress dependence of anisotropic flow through rock fracture with heterogeneous aperture distribution. *Earth and Planetary Science Letters*, 281(1):81–87, 2009.
- [12] H. Auradou, G. Drazer, J.P. Hulin and J. Koplik. Permeability anisotropy induced by the shear displacement of rough fracture walls. *Water Resour. Res.*, 41(W09423), 2005.
- [13] G. Izadi and D. Elsworth. Reservoir stimulation and induced seismicity: Roles of fluid pressure and thermal transients on reactivated fractured networks. *Geothermics*, 51:368–379, 2014.
- [14] I. Moeck, G. Kwiatek and G. Zimmermann. Slip tendency analysis, fault reactivation potential and induced seismicity in a deep geothermal reservoir. *Journal of Structural Geology*, 31(10):1174–1182, 2009.
- [15] H.S. Lee and T.F. Cho. Hydraulic characteristics of rough fractures in linear flow under normal and shear load. *Rock Mechanics and Rock Engineering*, 2002.
- [16] K.A. Lie. An introduction to reservoir simulation using matlab: User guide for the matlab reservoir simulation toolbox (mrst). *SINTEF ICT*, May, 2014.
- [17] E. Liu. Effects of fracture aperture and roughness on hydraulic and mechanical properties of rocks: implication of seismic characterization of fractured reservoirs. *Journal of Geophysics and Engineering*, 2(1):38, 2005.
- [18] R.L. Naff. On the nature of the dispersive flux in saturated heterogeneous porous media. *Water Resources Research*, 26(5):1013–1026, 1990.
- [19] J. Rutqvist. Fractured rock stress-permeability relationships from in situ data and effects of temperature and chemical-mechanical couplings. *Geofluids*, 15(1-2):48–66, 2015.
- [20] M.E. Thompson and S.R. Brown. The effect of anisotropic surface roughness on flow and transport in fractures. *Journal of Geophysical Research: Solid Earth*, 96(B13):21923–21932, 1991.
- [21] J. Rutqvist, C. Leung, A. Hoch, Y. Wang and Z. Wang. Linked multicontinuum and crack tensor approach for modeling of coupled geomechanics, fluid flow and transport in fractured rock. *Journal of Rock Mechanics and Geotechnical Engineering*, 5(1):18 – 31, 2013.